UC Merced
UC Merced Electronic Theses and Dissertations

Title

Hierarchical 3D Carbon Based Electrodes for Energy Storage and Conversion

Permalink

https://escholarship.org/uc/item/0c25g34k

Author

Hernandez, Yaneth Cristina

Publication Date

2022

Copyright Information

Peer reviewed|Thesis/dissertation

Hierarchical 3D Carbon Based Electrodes for Energy Storage and Conversion

A Thesis submitted in partial satisfaction of the requirements
for the degree of Master of Science in Materials and
Biomaterials Science and Engineering:

Yaneth Cristina Hernandez

Committee in charge:
Professor Jenifer Lu, Advisor
Professor Christopher Viney, Chair
Professor Min Hwan-Lee
2022

The thesis of Yaneth Cristina Hernandez is approved:

_____
Jennifer Lu, Advisor   Date

_____
Christopher Viney, Chair   Date

_____
Min-Hwan Lee   Date

Acknowledgments

Jeremiah 33:3 says:

"Call to Me, and I will answer you, and show you great and mighty things,
which you do not know."

Firstly, I would like to thank God for the opportunity of continuing my studies well into graduate school. Without his blessings and help this journey would have been a much more different path. I would also like to thank my family, in particular my grandfather for his continued support throughout the years, as well as my friends for all the help and support.

I also want to acknowledge my lab mates Jackie, Sam, Han Lin, Will, Michael and Katie for all of their help in the lab. Whether it was a small conversation about a particular research or class topic, collecting data or fixing instruments together; every single one of you have been a great part of my journey and I will be forever grateful for knowing each of you.

I would also like to acknowledge my mentors throughout my journey in the Lu lab. Thank you to Carlos Ortuno for teaching me how to be a good student in the lab even before I considered going to graduate school. Thank you to Jason Qian for being an amazing postdoc and teaching me new tricks around the lab as well as how to be a more efficient graduate student. Thank you to Dr. Viney for his help when I was preparing to take the GRE exam before applying to graduate school and for his enthusiasm in classes that made learning about the subjects a fun experience.

And without further ado thank you to my mentor Dr. Jennifer Lu. This has been a long journey for the both of us. Filled with setbacks, disagreements, learning experiences, joyful times and more. Over the years I have learned a lot from you. Being part of your lab is what made me be more interested in pursuing the energy storage and conversion field. Although my time with you at UC Merced has come to an end, I will always be grateful for all the things that you have taught me. Thank you for everything, it has been an honor.

<p style="text-align:center">Table of Contents</p>

List of Figures and Schemes

Abstract

Renewable energy is regarded as the most effective tool to combat climate change/global warming. Electrochemical reactions are the cornerstone for these technologies. I present a fabrication process to create hierarchical structures with engineered functional groups (redox species for repeated electrochemical reactions or catalyst species for electrochemical reactions) uniformly distributed on an electrode aiming for enhanced device performance. For energy storage applications, poly (1,5- diaminonaphthalene) (PDAN) and polyaniline (PANI) have been oxidatively electrografted onto carbon for side-by-side comparison. It has been found that PDAN offers 17% higher theoretical capacitance than PANI. More impressively due to the rigid highly conjugated nature PDAN has a more stable cycle stability than PANI. This lightweight platform with high energy density and enhanced cycle stability opens the door to a wide array of electrochemical storage applications. For energy conversion applications, metal-nitrogen coordinated species are a low-cost alternative to platinum. In this study poly (4-vinylpyridine) (P4VP) has been cathodically electrografted onto carbon substrates. The effect of ligands and metal species on coordination and catalytic activity was investigated by keeping all other parameters (interface properties, spatial distribution, and relation with electrodes) the same. Cobalt-containing catalysts have demonstrated the best catalytic activity compared to tin and iron-based catalysts. This platform is expected to provide a tool to screen a variety of catalyst systems.

Introduction

With the growing concern for climate change, geopolitical issues and increased reliance on electronic devices renewable energy has become an increasingly hot topic among the scientific community. However, as of now fossil fuels are still the largest source of energy in the US. In 2021 79% of the energy needs of the US were covered by fossil fuels while only 12% was covered by renewable energy, the remaining 9% came from nuclear energy[53]. Although the vast majority of energy in the US comes from fossil fuels that does not mean that there is no hope for renewable energy. Everyday scientists make strides to have more energy be provided by renewable energy sources. Just a few weeks ago, the state of California was able to provide energy to the entire state with solely renewable energy sources for 3 minutes interrupted[54,55]. There are a variety of renewable energy technologies available such as solar systems, batteries, wind turbines and so on. Renewable energy will be key to powering our world in the upcoming years. Although we can generate renewable energy, we also need to have the capacity to store for when we need it. Batteries and pseudocapacitors can store this energy. In particular, pseudocapacitors are ideal for fast charge discharge applications. These devices are able to store energy in the chemical form through redox reactions. In the other hand we can also generate energy by using hydrogen, a very lightweight and clean fuel, in fuel cells. Fuel cells have the ability to convert electrochemical energy into electricity. These devices are great for applications that require a lot of power delivered such as powering a bus or a large transportation truck. In this study we use hierarchical 3D structures coated with redox active material to make electrodes for energy storage and energy conversion applications. We will first look at pseudocapacitors for energy storage. Then we will look at the use of catalysts for energy conversion in fuel cells.

Pseudocapacitors fall under the umbrella of supercapacitors. Supercapacitors are different from capacitors because these devices are able to have much higher capacitance values than those of capacitors[56-58]. Pseudocapacitors are classified as supercapacitors because of this. For pseudocapacitors the primary energy storage mechanism comes from redox reactions[59,60]. This is why pseudocapacitors are often composed of metal oxide or conductive polymer materials[60-63]. These materials are often able to reach high capacitance values, however, they are often plagued by poor rate capabilities due to poor cycle stabilities[64,65]. Due to this my research focused on a highly stable conductive polymer Poly-(1,5-diaminonaphthalene) or PDAN. This conductive polymer stands out from others such as polyaniline (PANI) due to its great cycle stability. The conjugated nature of the polymer makes it rigid and prevents mechanical failure that rises from the redox reactions that the polymer undergoes to store energy[64]. So, in this research not only were we able to achieve a high capacitance, 17% higher than PANI, we also were able to achieve a high cycle stability. Now that we have addressed how to store our energy, let's talk about how to produce our energy with fuel cells.

Fuel cells have become a promising source of clean energy as they produce electricity by consuming oxygen and hydrogen[66]. The only byproducts of this cell are water and heat. PEM fuel cells are energy conversion devices that consist of an anode, cathode, electrolyte, the proton exchange membrane, and a

catalyst[67,68]. Although fuel cells have promise they have a major setback. Fuel cells require a catalyst in order to accelerate the sluggish kinetics of oxygen reduction reactions (ORR) that occurs at the cathode. The most commonly used catalyst for fuel cells is platinum[67,69]. Although platinum gives a great electrochemical performance for ORR the catalyst itself can be very costly and it is prone to leaching and poor cycle stability[70]. Because of this there has been a lot of research to replace platinum. As of now there has been some promising catalyst replacements such as carbon-metal-nitrogen (M-Nx-C) coordinated catalysts[71-75]. In this work Poly(4-vinylpyridine) (P4VP) was used as a nitrogen source to synthesize M-Nx-C catalysts. First a systematic study of the effects of ligands on coordination chemistry was conducted. Followed by an investigation on ORR catalytic performance of said ligands and as well as various metal species. In this work we found that the type of ligand affects the coordination chemistry. We also found that cobalt containing catalysts had a better overall performance when compared to iron and tin containing catalysts.

The work contained in this thesis work can be of use to both the energy storage and conversion fields. In the energy storage front we present a pseudocapacitor with high capacitance and high cycle stability. While on the energy conversion side we present a platform in which to test a variety of metal precursors with promising ORR catalytic activities. The hope is that this work will be of use for a multitude of applications in the renewable energy world.

Chapter 1: Poly(1,5-diaminonaphthalene)-Grafted Monolithic 3D Hierarchical Carbon as Highly Capacitive and Stable Supercapacitor Electrodes

1.1. Introduction

Over the last two decades, handheld electronics have gained increasing applications for sport activities, health monitoring, biomedical sensing, environmental detection among other applications.[1–6] These emerging applications call for a lightweight energy storage system that can safely operate over an extended period of time. At the same time, load leveling of renewable energy, harvested from solar and wind farms, as examples, also requires energy storage systems that offer adequate cycle stability without any safety concerns.[7]

Li-ion based batteries use flammable electrolytes to provide high energy density.[8] In addition to safety concern, these batteries suffer from limited power density and cycle performance.[9,10] Comparatively, supercapacitors exhibit higher power density, significantly prolonged cycle life and can operate in a safe aqueous electrolyte that is non-flammable and environmentally benign. To address the intrinsically low energy density of supercapacitors, an immense effort has been made to incorporate redox active centers into supercapacitors to form pseudocapacitors.[10]

Redox-active conjugated polymers that consist of electrochemical active sites in each repeat unit offer appreciable theoretical capacitance and electrical conductivity.[11–16] Compared to inorganic redox materials such as transition metal oxides and sulfides, they exhibit dramatically enhanced mechanical flexibility and processibility.[14,15,17] Therefore, these polymers can be readily deposited on a flat or curved surface. In addition, they are lighter in weight and can be processed inexpensively.[14] However, the application of conventional conjugated conductive polymers in energy storage is hindered by two major drawbacks. One is poor cycle stability brought by significant volumetric changes during doping and de-doping of ions in the charge and discharge processes.[18] The other is reduced specific capacitance and rate capability with polymer thickness due to the combination of the inability to timely transport ions to reaction sites and increased electron transport length.[19,20]

To boost electrical conductivity and shorten diffusion length, polyaniline (PANI), as an example, is often mixed with carbon allotropes.[11,13,21] Nevertheless, stochastic blending with carbon brought about ill-defined structures which cannot provide continuous electron transport pathways and stymie ion diffusion as well.

Polydiaminonapthalene (PDAN), which can be viewed as two anilines fused together, has not received similar attention in comparison to PANI. 1,5-diaminonaphthalene, 1,5 DAN hereafter, can be polymerized oxidatively in aqueous and organic electrolytes[22–28] to form poly(1,5-diaminonaphthalene) 1,5 PDAN (Scheme 1a) in linear or ladder form.[23,26] It is known that conjugated ladder polymers exhibit extraordinary chemical, and mechanical stability.[29, 30]

Due to chemical structural resemblance of 1,5 PDAN and PANI, one follows previously reported approaches to calculate theoretical capacitances.[21] The theoretical capacitance of 1,5 PDAN using the ladder structure would be 1545 F/g whereas that of PANI is 1325 F/g. Therefore, 1,5 PDAN offers 17 % higher specific capacitance.

We herein report a holistic approach to form a reproducible 3D electrode in which a layer of 1,5 PDAN is monolithically integrated with mechanically robust high-density carbon nanotubes (CNTs) grown on carbon cloth, CNTs-a-CC. Without any special treatment, 1,5 PDAN can be conformally deposited onto each individual CNT. To the best of our knowledge, this is the only conductive polymer system that can uniformly deposit redox centers in carbon by a simple electrochemical oxidation step.[31]

The specific capacitance of 1,5 PDAN based on multiple sample analysis is in the range of about $900 - 1250$ F/g ($0.07 \sim 0.5$ mg/cm^2), on par with, if not exceeding, well-studied conjugated polymers such as PANI and polypyrrole (PPy).[13,32] Impressively, this value can be maintained at a high rate, 100 mV/sec. The unobstructed ion and electron transport pathways offered by this new hierarchical structure combined with uniform dispersion of 1,5 PDAN throughout the entire CNTs-a-CC framework gives this impressive result. Electrochemical reactions in 3D, produce a capacitance of 650 F/g under 2 mV/s scan rate at a mass loading of 2.5 mg/cm^2 of 1,5 PDAN.

The relation between weighed mass and calculated mass using charge flow during polymerization, explicitly indicates the formation of the ladder structure. Due to extended conjugation, 94 % capacitance retention is obtained after 25,000 cycles at 100 mV/s scan rate, a value significantly higher than what has been observed from most conductive polymer systems.[12]

Through seamless integration of PDAN with CNTs-a-CC, this platform simultaneously offers enhanced theoretical capacitance, and improved polymer loading for energy density and power density. The significantly enhanced cycle stability owing to structurally robust CNTs-a-CC together with mechanically and chemically stable PDAN has been demonstrated.

This new energy storage platform has the potential to be incorporated into textiles, wearable electronics, and gadgets. The methodology to fabricate 3D hierarchical electrochemical systems is scalable, reproducible, and thus manufacturable. This lightweight and flexible electrode platform circumvents the use of the traditional heavy metal current collectors and eliminates the need for binder that can block electrochemical reactions. The hierarchical platform can serve as an inspirational model to disperse functional species in 3D for enhanced rate capability and density. Furthermore, this platform can be extended to host electrocatalysts for energy conversion reactions or electrochemical sensors for sensing applications.

1.2. Experimental Methods

1.2.1. Material synthesis

1.2.1.1. Carbon cloth modification. Plain carbon cloth (CC) that is made of an average of 10 μm microfiber was purchased from Fuelcell Earth. Initially, CC samples were annealed in 5 % O_2 / 95 % Ar at 400 °C for 2 hours to remove organic contaminants and incorporate oxygen species on the carbon surface. The CC samples were cut in 1 inch x 8 inch size and treated with 5 M HNO_3 to enhance hydrophilicity further. After washing HNO3 treated CC samples in deionized water, KOH impregnations were conveyed with a degassing process to wet and fill all of the accessible surface with 8 M KOH. The samples were then rolled to fit into 1 inch alumina tubes and pushed into the heating zones. The KOH activation process was conveyed at 825°C for 3 hours and cooled to room temperature. KOH activated CCs (a-CC) were then sonicated in 1M HCl for 24 hours to remove side products.

1.2.1.2. Catalyst deposition and carbon nanotube growth. CNT growth on CC and a- CC were proceeded in a quartz tube via chemical vapor deposition (CVD) method. For the CNT synthesis, copper and nickel catalysts were deposited alternately via electroplating using solutions of 4 mM $CuSO_4$ and 40 mM $NiNO_3$ at constant potentials of 0.04 V and -0.56 V vs saturated calomel electrode (SCE) for 8 s and 20 s respectively. The plating potentials were selected based on the reduction potentials of Cu and Ni ions at a pH of 3. The catalyst coated CC and a-CC were dried in a vacuum oven and then moved to a CVD furnace. Samples were heated with Ar/H_2 carrier gas and held at 650°C for 15 minutes for the formation of Ni/Cu nanoparticles. Then, CNT growth was carried out at 725°C with a flow of ethylene for 20 minutes. After the CVD growth, samples (CNTs-a-CC) were treated with 1 M HNO_3 for 2 hours to remove any residual catalyst and amorphous carbon. The typical loading of CNTs on a-CC is 3 mg/cm^2. Electrochemical depositions and analyses were conducted with Biologic potentiostat by using three electrode electrochemical cell setup. For the Cu/Ni catalyst deposition, SCE as a reference electrode and a nickel plate as a counter electrode were used specifically.

1.2.1.3. Electro-oxidative polymerization of 1,5 PDAN. 1,5 DAN monomers were purified by ethanol recrystallization process before use. For oxidative polymerization, three-electrode electrochemical cell was used with a counter electrode (graphite) and a reference electrode (Ag/AgCl). Electropolymerization processes were conducted via potential sweeping or pulse deposition between potentials of 0 V – 1.2 V with respect to reference electrodes in acid. On each cycle of pulse deposition, potentials were kept at 1.2 V for 20 seconds. In aqueous solutions, 10 mM 1,5 DAN monomers were dissolved in 0.02 M $NaClO_4$ as supporting electrolyte and 0.1M $HClO_4$ solution. In acetonitrile solutions, 10 mM 1,5 DAN monomers were dissolved with 0.1 M $NaClO_4$ as supporting electrolyte.

1.2.1.4. Electro-oxidative polymerization of PANI. Aniline monomers were initially purified, and above-mentioned oxidative polymerization was performed. Electropolymerization processes were conducted on a-CC via pulse deposition between potentials of 0 V – 1.2 V with respect to reference electrodes in 1 M H_2SO_4 solution. Two sets of aniline monomers with 0.02 M and 0.1 M monomers concentration were polymerized with 20 successive pulses where potentials kept at
1.2 V for 20 s. After polymerization, electrodes were rinsed in DI water and oligomers removed in acetone solution.

1.2.2. Characterization

1.2.2.1. Electrochemical Characterization. For electrochemical analyses, a carbon rod as counter electrode and a saturated calomel (SCE) reference electrode were used in
0.5 M H_2SO_4 electrolyte. Cyclic voltammetry analyses were conveyed with different scan rates between 2 mV/s and 100 mV/s. Galvanostatic charge discharge analysis was conducted with current rates of 1 A/g, 2 A/g, 4 A/g, 8 A/g and 16 A/g. Cycle stability tests were conducted by using cyclic voltammetry analyses with $Hg/HgSO_4$ reference electrode. Electrochemical impedance spectroscopy (EIS) analysis was investigated at frequencies between 0.01 Hz and 100 kHz at 10 mV amplitude at fixed potential of 0.2 V vs. SCE reference electrode.
   Specific gravimetric and areal capacitances were calculated from the area in the cyclic voltammetry plots by using the following formulas:

$$C_g = \frac{\int I\, dV}{2vmV} \tag{1}$$

$$C_A = \frac{\int I\, dV}{2vAV} \tag{2}$$

where C_g is gravimetric capacitance (F/g), C_A is areal capacitance (F/cm^2), I is current (A), v is scan rate (V/s), m is mass (g), V is potential range and A is electrode surface area (cm^2). Additionally, specific capacitances from galvanostatic charging/discharging plots were calculated by using the following formula:

$$C_g = \frac{I * t}{m * V} \tag{3}$$

where C_g is gravimetric capacitance (F/g), I is discharging current (A), m is active mass (g), V is potential range and t is discharging time.

1.2.2.2. Structural Characterization. Field Emission Scanning Electron Microscopy (FESEM, ZEISS GEMINI 500) was used to study morphological structures of carbon, 1,5 PDAN and PANI. For a fair comparison, identical samples were imaged before and after electropolymerization or stability tests.

Polymerization of 1,5 DAN monomers was confirmed by Fourier-Transform Infrared Spectroscopy Attenuated Total Reflectance Analyses (FTIR-ATR) through Bruker Vertex 70 spectrometer. FTIR-ATR spectra were recorded with absorbance spectra.

1.3. Theoretical Calculations

1.3.1. Theoretical capacitance of 1,5 PDAN

The oxidation states of 1,5 PDAN are shown at Scheme 1b. Excellent electrochemical performance is mainly attributed to two fused aniline benzene rings. The theoretical specific capacitance of PANI was calculated using the equation:

$$C_T \ = \frac{\alpha * F}{\Delta V * M_w} \tag{4}$$

where α is the number of electrons involved in the redox conversion of a single monomer unit, F is Faraday constant, ΔV is the potential window and M_w is the molecular weight of each monomer.[21,34] As a result, the theoretical specific capacitance of PANI would be 1325 F/g for 0.8 V potential window, calculated by using Equation 4, assuming that one electron is transferred per aniline unit. If one applies a similar approach to 1,5 PDAN, 1545 F/g is obtained, assuming that two electrons transfer per 1,5 DAN unit for the ladder structure formation. Therefore, 1,5 PDAN intrinsically possesses higher theoretical pseudocapacitance, 17 % higher than PANI. In this study, the pseudocapacitive behavior of 1,5 PDAN was analyzed by incorporating them onto a highly porous 3D carbon scaffold.
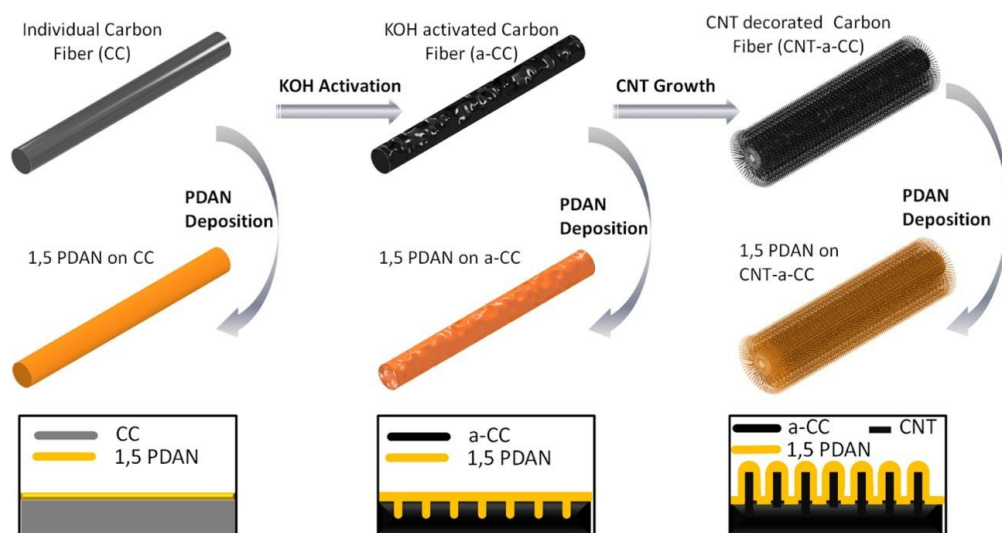
Figure 1. Schematic of process flow to fabricate a hierarchically nanostructured electrode starting from as-received carbon cloth to 1,5 PDAN grafted CNTs-a-CC.

1.4. Results and Discussion

Figure 1 illustrates the electrode fabrication process flow. The carbon cloth was first subjected to a surface modification via KOH activation, followed by catalyst precursor deposition and finally CNT growth. 1,5 PDAN was then electrografted to form the final hierarchical structure.

1.4.1. 3D scaffold formation and characterization

CC is a woven fabric consisting of microfibers with a smooth surface as shown in Figure 2a-b. CCs have very low surface area (e.g., 5.5 m^2/g) which can be improved with addition of nanostructured materials. It is known that the chemical vapor deposition of 1D carbon nanostructures proceeds through the decomposition of carbon precursors on transition metal catalyst seeds.[34–41] Catalyst seeds can be deposited via electrodeposition[36,37], e-beam evaporation[37] or solution impregnation methods.[38] Uniform catalyst distribution on carbon microfibers is the prerequisite for the formation of evenly distributed CNTs, but it is challenging. To obtain uniform catalyst coverage on carbon cloth, we modified the previously published method.[35] Ni and Cu were electrochemically deposited on carbon cloth due to the ability of Ni-Cu alloy catalysts to produce CNTs with a higher graphitic content than pure Ni (Figure S1).[29].

Prior to CNT growth, H_2 treatment at 650 °C was carried out to ensure the formation of metallic Ni-Cu alloy nanoparticles. At this temperature, the dewetting of the plated layer from the carbon surface renders the formation of catalyst nanoparticles anchored to the a-CC surface in the in the small pores developed during KOH activation (Figure S2). Non-uniform CNT growth was observed on bare CC as shown in Figure 2c. The reason behind the lack of growth is that small seeds are difficult to form on a smooth carbon surface through the dewetting method in the absence of a sufficient support. KOH interaction with carbon reduces K ions to metallic potassium at elevated temperatures while simultaneously oxidizing the carbon. Micro- and meso-porosity is developed due to the gasification of carbon and intercalation of metallic K, which is utilized as a catalyst support[42]. SEM images (Figure 2d-1) clearly support that pore formation after KOH activation.

CNTs grown on a-CC possess an average diameter of 50 nm, while up to 3 mg/cm^2 of CNTs were grown on each sample. Samples were treated with 1 M nitric acid to remove exposed residual catalyst seeds and amorphous carbon (Figure S3). For further improvement, the newly formed 3D current collector in which CNTs uniformly emanating from each carbon microfiber was coated with redox centers. Pertinent to this investigation, 1,5 PDAN was chosen as redox centers for enhanced energy storage performance.
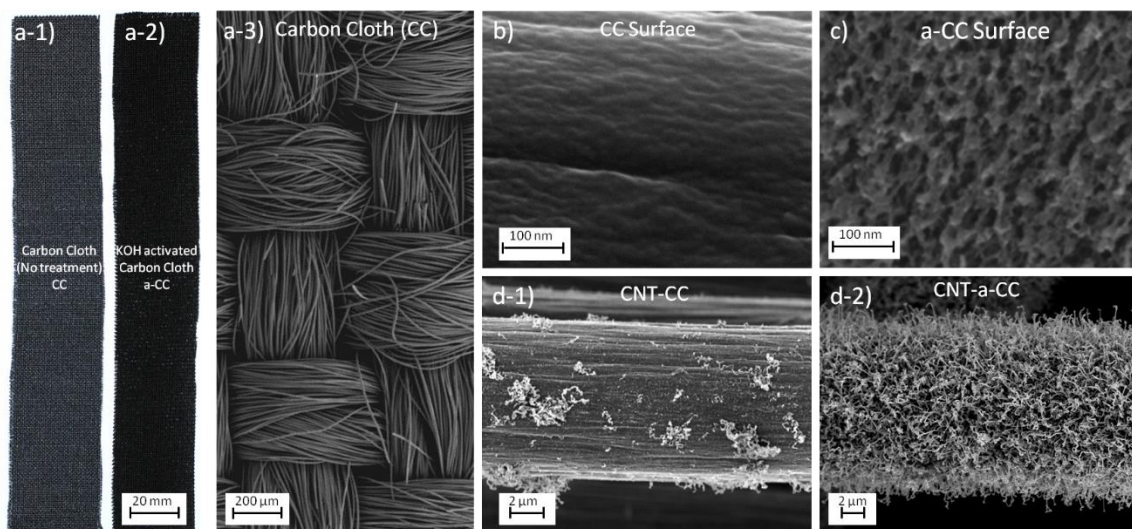
Figure 2. **(a)** Optical images of carbon cloth before and after KOH activation. SEM images of **(b)** carbon cloth threads, **(c)** a-CC surface, **(d-1)** no CNT growth on CC, **(d-2)** CNT growth on a-CC.

1.4.2. Electrografting 1,5 PDAN.

During polymerization, amines in DAN act as nucleophiles to react with the two oxidized phenyl rings.[23,25,43] Electropolymerization proceeds via one- or two-electron transfer per monomer (Scheme 1a). 1,5 DAN is not soluble in water, but its solubility increases after protonation of amine groups by an acid such as $HClO_4$. Electropolymerization was carried out in an acidic solution containing $HClO_4$ (pH=1). As shown in the CV curves in Figure S4, an irreversible oxidation peak was observed at 0.72 V vs. Ag/AgCl at first scan. The intensity of the irreversible peak decreases with increasing cycles due to monomer consumption. There are two pairs of reversible redox peaks observed 0.35 and 0.5 V vs. Ag/AgCl after the first cycle due to the polymer formation. The intensity of the reversible peaks increases with cycle.
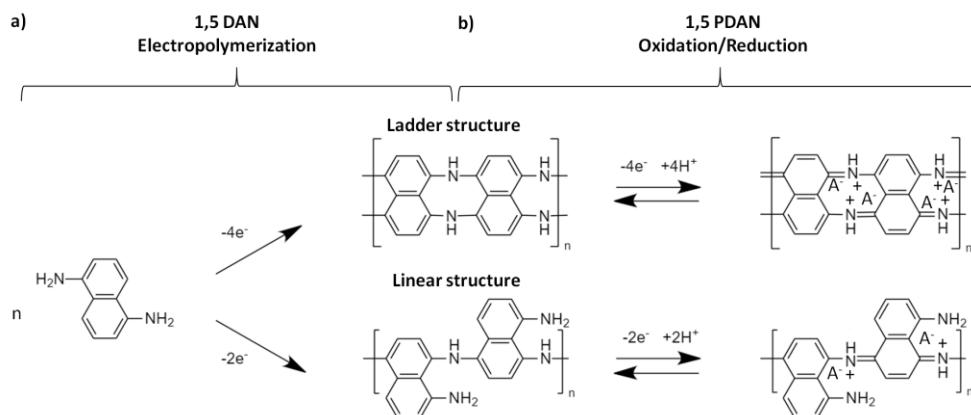
Scheme 1. (a) Proposed polymerization scheme for ladder and linear structure. **(b)** Redox reaction of PDAN for ladder and linear structure.

17

We demonstrated that 1,5 PDAN can be grafted conformally onto CNTs-a-CC (Figure 3 and Figure S5). Polymer mass loadings were 0.3 mg/cm^2, 1.05 mg/cm^2, 1.53 mg/cm^2 and 2.5 mg/cm^2, corresponding to film thicknesses of 12.8 nm, 41.4 nm, 66.6 nm and 87.2 nm, for 5, 20, 40 to 80 pulse depositions, respectively (Figure S5). According to SEM images, polymerization in acids yields rough, granular surfaces (Figure 3c-d) which could offer a greater surface area leading to enhanced supercapacitor performance. On the other hand, 1,5 PDAN films grown using acetonitrile are densely packed (Figure 3e-f). The measured polymer loadings in acetonitrile were 0.28 mg/cm^2, 0.45 mg/cm^2 and 0.8 mg/cm^2 for the polymerization cycle of 5, 10 and 40 respectively and corresponding film thicknesses increase gradually (Figure S6). Despite similar mass gain observed at low loading (5 cycles), there was a limited growth at high loadings (40 cycles). We attribute this to a lower polymerization efficiency to the solubility of oligomers in acetonitrile, which was observed to change the color of the monomer solution red in the vicinity of the working electrode.[24]
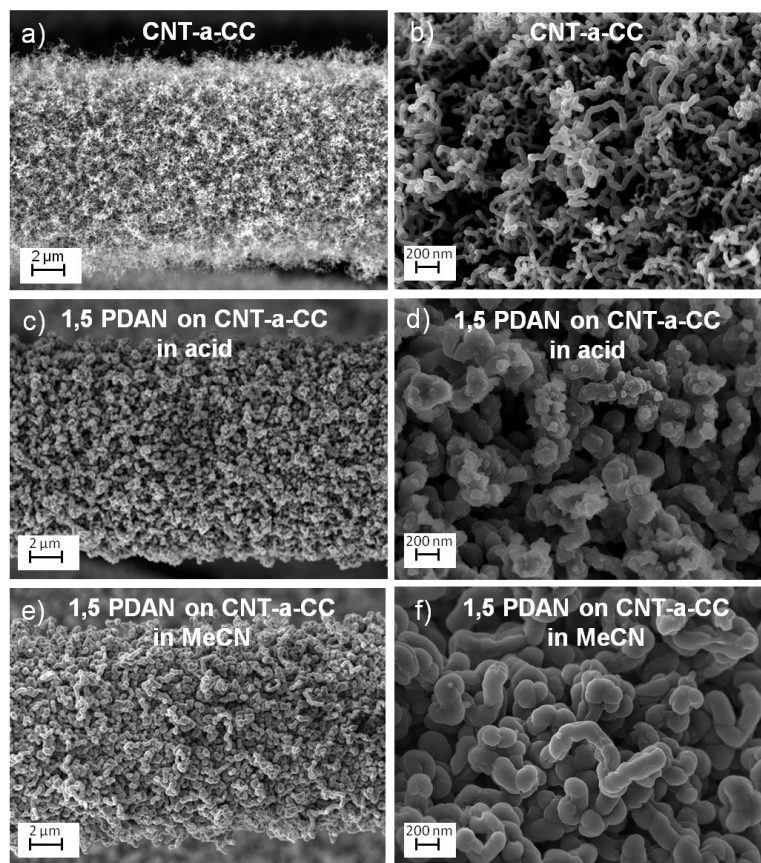
Figure 3. **(a-b)** SEM images of CNT decorated activated carbon cloth, 1,5 PDAN grafted CNTs-a-CC in acid **(c-d)** and in acetonitrile **(e-f)**.

To confirm the polymer formation, FTIR analysis was conducted. The three absorption bands near 1585 cm^{-1}, 1510 cm^{-1} and 1410 cm^{-1}, observed in the FTIR spectrum of DAN (Figure S7), resulted from stretching vibration of C-C on the

aromatic rings.[23,28,44] The broadening of these peaks observed from the polymer spectrum (Figure S7), indicates the formation of the polymer.[44] The disappearance of C-N stretching vibrations of the aromatic primary amine around 1360 cm^{-1} for DAN monomer is the indication of the polymer formation.[28,44]

As for N-H stretching vibrations in the region of 3450 - 3200 cm^{-1}, the monomer shows bands around, 3413, 3322 and 3223 cm^{-1} corresponding to symmetric and antisymmetric NH2 vibrations, respectively. The polymer counterpart shows a broadening band around 3337 cm^{-1} associated with N-H stretching mode for secondary amine groups, which can be attributed to disappearance of NH2 groups that were consumed in the polymerization process and further supports the polymer formation.[23,28] The structure of 1,5 DAN monomers and possible structures of 1,5 PDAN polymer are depicted at Scheme 1a with a ladder structure and linear structure.[23]

1.4.3. Accurate determination of supercapacitor electrode mass and the effect of morphology on mass loading

An accurate mass determination is important for specific capacitance calculation. The large discrepancy in performance in the literature for materials such as PANI is in part due to the inability of accurate mass determination.[33] It is challenging to determine a miniscule mass gain resulting from polymer grafting, especially with consideration of the loss of material (*e.g.,* carbon nanotubes and carbon threads from carbon cloth) during the fabrication process. Alternatively, charge flow during polymerization has been used to calculate the thickness of a deposited polymer layer[45] and to estimate the gravimetric capacitance.[24,46] Assuming 100 % polymerization yield no charge loss and charges were consumed to form the deposited polymer), there should be a linear relation between charge flow (Q) and polymer mass (m):

where M^w is the molecular weight of the repeat unit, F is the faraday constant, n is the number of electrons needed for each monomer to participate in polymerization. Typically, n varies with monomer type and polymerization conditions. For example, n is 2 for linear structure and n is 4 for ladder structure (Scheme 1).[26,47,48]

To determine n, equation 5 is used by taking "m" as weighed mass. n was calculated to be about 4 – 5.5 electrons per monomer when DAN polymerized in acid (Figure 4a). Given that high electropolymerization yield in acid, this finding supports a significant percentage of the ladder structure formed.[26,47,48] On the other hand, the calculated n is around 18 electrons per monomer in acetonitrile. Such discrepancy can be attributed to DAN oligomers formed and the subsequently dissolved in the acetonitrile which is a good solvent for DAN oligomers. Such low efficiency was observed with 1,8 PDAN polymerization in acetonitrile medium.[24] Due to the high polymerization efficiency and the loosely packed 1,5 PDAN obtained by pulse

electrodeposition in acidic media (Figure 3d), this method was chosen for the investigation of the effect of the morphology of the current collector on performance.
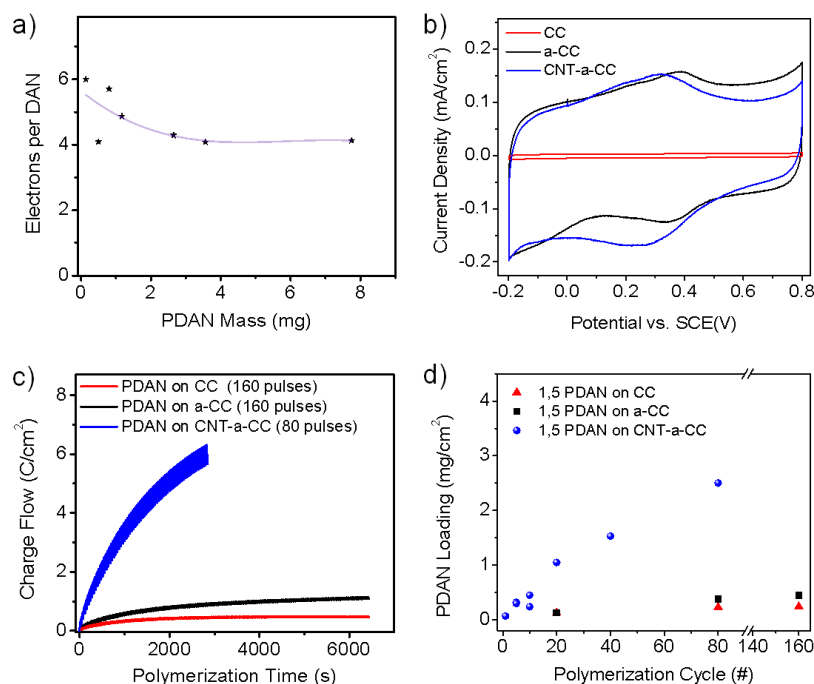
Figure 4. (a) The corresponding number of electrons used during polymerization with various 1,5 PDAN loading in acidic solution. **(b)** Electrochemical charge storage comparisons of bare CC, a-CC, CNTs-a-CC. Charge flow during electropolymerization **(c)** and polymerization cycle vs 1,5 PDAN loading **(d)** on CC, a-CC and CNTs-a-CC.

Charge flow allows real-time monitoring of mass gain during polymerization, polymer deposition rate on CC, a-CC, CNTs-a-CC was carefully investigated. Based on cyclic voltammetry analysis (Figure 4b), specific capacitance of CC, a-CC, CNTs- a-CC was 0.05 F/g, 2 F/g, and 1.5 F/g respectively at 5 mV/s scan rate. A slight reduction after CNT growth might be due to clogging of nanopores created by KOH activation. Morphology can significantly impact polymer deposition rate (Figure 4c). For CC and a-CC, the charge flow increases during the initial several cycles and then reach to plateau indicating that the maximum loading is reached. The maximum PDAN loading on CC and a-CC are 0.24 mg/cm^2 and 0.48 mg/cm^2 respectively. In a stark contrast, for CNTs-a-CC, 2.5 mg/cm^2 PDAN loading has been obtained without saturation (Figure 4d). 1,5 PDAN deposition rate on CC, a-CC and CNTs-a-CC is 0.01 mg/cm^2, 0.02 mg/cm^2 and 0.066 mg/cm^2 for each cycle respectively.

1.4.4. Electrochemical performance

A thin polymer coating that mitigates performance loss resulting from ionic diffusion and electrical conductivity would provide a gravimetric capacitance value that is close

to the theoretical one. CNTs-a-CC was chosen for the investigation of 1,5 PDAN electrochemical charge storage behavior,

The thinnest 1,5 PDAN coating was obtained by decreasing the monomer concentration (5 mM DAN) and polymerization time (20 seconds, 2 pulses), yielding the areal mass density of 1,5 PDAN of 0.07 mg/cm^2 that was confirmed based on charge flow calculation. CV analyses show two pairs of reversible redox peaks at 0.12 V and 0.44 V vs. SCE (Figure 5a). The observed reversible redox pairs are ascribed to the oxidation and reduction of the ladder structure (as shown in Scheme 1b).

To investigate the charge storage mechanism, the redox peak potentials and intensities were compared with various scan rates.[49] Both anodic peak currents for
0.12 V (peak 1) and the minor one at 0.44 V (peak 2) increase linearly with respect to scan rate as shown in Figure 5b-c. The peak currents are proportional to $v^{0.95}$ which indicates that charge storage is governed by surface-controlled redox reactions. This result showcases the importance of the combination of low tortuosity of CNTs-a-CC with thin conformal coating of PDAN. Corresponding specific capacitance of 1,5 PDAN is 1250 F/g which can be maintained up to 100 mV/s scan rate (Figure 5e). This experimental value is very close to the theoretical value of 1545 F/g for the ladder structure.

We decoupled the faradic component from the double layer region (Figure 5d). Introduction of 2% PDAN yielded 1.4 times increases of the total capacitance. Corresponding specific capacitance of 1,5 PDAN is 1250 F/g which can be maintained up to 100 mV/s scan rate (Figure 5e). This experimental value is very close to the theoretical value of 1545 F/g.

To further verify our finding, we prepared additional 6 samples with a thicker coating of 0.1 – 0.5 mg/cm^2. Figure 5f is a histogram for 7 samples on CNTs-a-CC. The specific capacitance ranges from 900 to 1250 F/g. The median is 1100 F/g. This finding further buttresses the contention of high percentage of ladder structure.
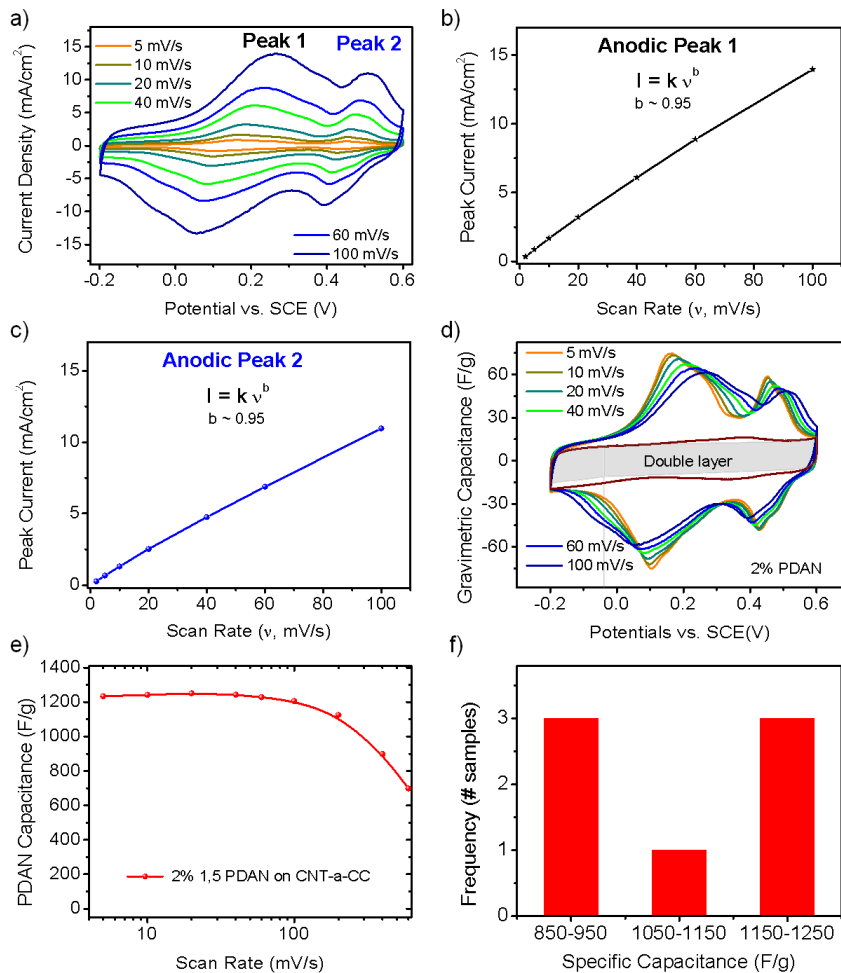
Figure 5. (a) Cyclic voltammetry analysis of thin 1,5 PDAN on CNTs-a-CC. Corresponding anodic peak currents at different scan rates for Peak 1 **(b)** and Peak 2 **(c)**. **(d)** Total capacitance of 1,5 PDAN electrodes at different scan rates. **(e)** Pseudocapacitive contribution from 1,5 PDAN at different scan rates. **(f)** Specific gravimetric capacitance on CNTs-a-CC for loadings of $0.1 - 0.5$ mg/cm^2.

The overall capacitance increases with 1,5 PDAN loading (Figure 6a). We further investigated the energy storage capability of thicker 1,5 PDAN coatings on CNTs-a-CC. This structurally well-defined and mechanically robust 3D carbon platform allows for more deposition of redox active species than flat or porous surfaces. The original areal capacitance of CC was 5 mF/cm^2 at 2 mV/s. At a loading of 2.5 mg/cm^2 1,5 PDAN on CNTs-a-CC, the areal capacitance increased to 1600 mF/cm^2 at 2 mV/s (Figure 6b) and corresponding capacitance contribution of 1,5 PDAN is found to be 650 F/g at 2 mV/s (Figure 6c). The specific capacitance of 1,5 PDAN on CNTs-a-CC with different loadings in an acidic medium is summarized in Figure 6d. The results highlight the importance of a 3D open structure for achieving excellent gravimetric capacitance at a high polymer loading.

22
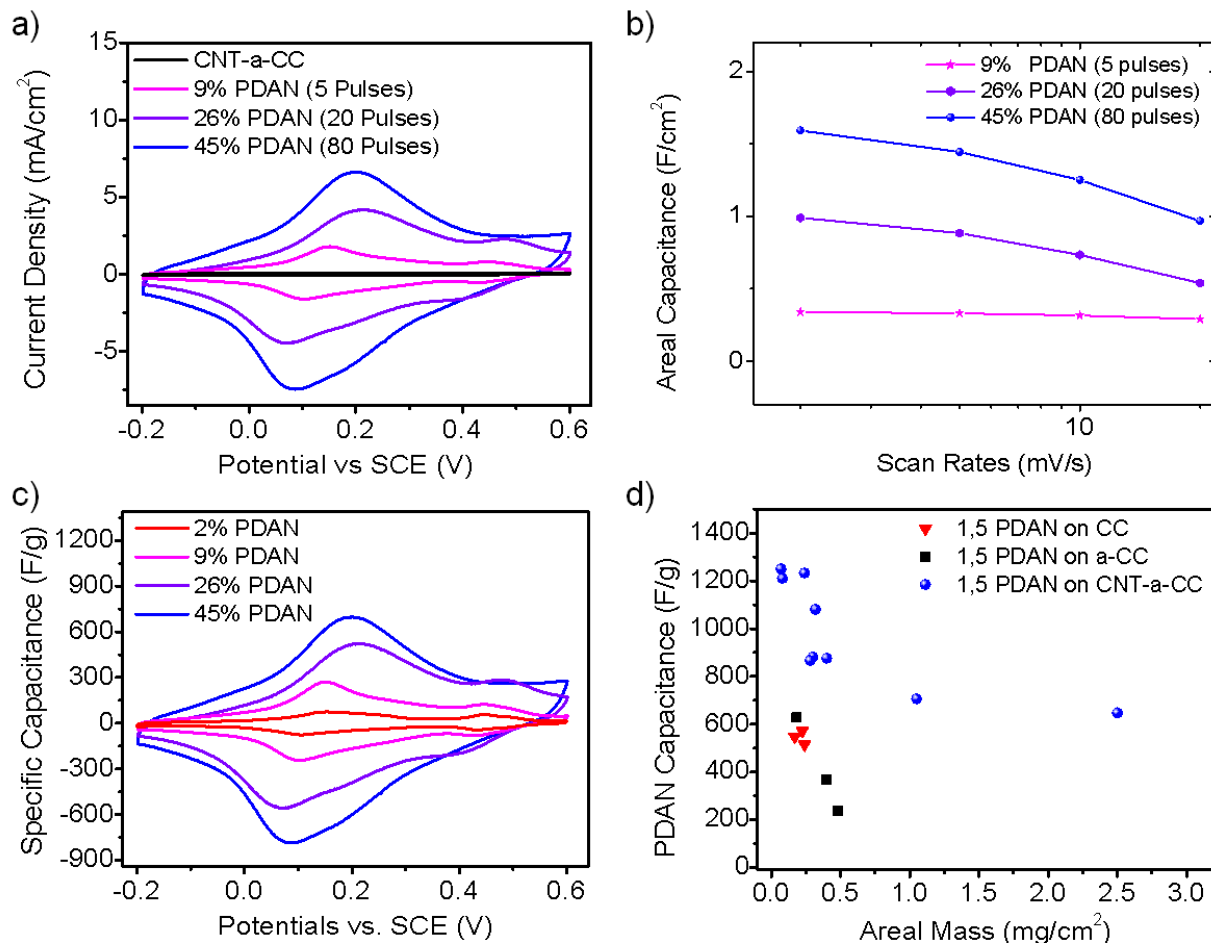
Figure 6. **(a)** CV characteristics of 1,5 PDAN on CNTs-a-CC at 2 mV/s with different polymer loadings, **(b)** Areal capacitance comparison with various scan rates,
(c) Electrode capacitance and **(d)** Specific capacitance of 1,5 PDAN synthesized on CC, a-CC and CNTs-a-CC with different areal masses.

The substrate morphology plays an important role in electrochemical storage (Figure 6d and Figure S9). Although the accessible surface area on a-CC is comparably 40 times higher than CC, the electrochemical performance of 1,5 PDAN on a-CC was mediocre. The polymer deposition planarizes porous surfaces (Figure S10). Since CNTs-a-CC offers 30 times higher surface area than that of CC, it allows the deposition of 10 times more polymer while still maintaining appreciable electrochemical energy storage capability. To maintain 650 F/g of PDAN, CNTs-a-CC allows 2.5 mg/cm^2 of 1,5 PDAN loading whereas less than 0.25 mg/cm^2 polymer loading on CC and on a-CC which is 10 times less is permitted.

Galvanostatic charge discharge analyses of 1,5 PDAN on CNTs-a-CC (Figure S11) confirms the pseudocapacitive nature of 1,5 PDAN. Furthermore, electrochemical impedance analysis indicates nearly ideal capacitive behavior of 1,5 PDAN on CNTs-a-CC at a load of 2.5 mg/cm^2 (Figure S12). The two-cell performance using the porous carbon as a negative electrode was characterized in 0.5 M H$_2$SO$_4$ in 1.6V potential window. The electrochemical energy storage capacity of PDAN is F/g at 2 mV/sec (Figure S13).

23

The stability analysis was conducted for 1,5 PDAN as shown in Figure 7. 1,5 PDAN shows exceptionally high capacitance retention (94%) after 25000 cycles at 100 mV/s scan rates, compared to other conductive polymers.[13] PANI was electropolymerized on a-CC. We compared cycle stability (Figure S14). Unlike 1,5 PDAN, the reduction of electrochemical surface, indicates the degradation of PANI. SEM images (Figure S15) showed nanofiber-like PANI deposition which were either dissolved or detached from a-CC after the cycle stability test. The observed mechanical degradation is a common stability problem for conductive polymers due to repeated swelling and de-swelling during the redox reaction.[50] In contrast, no structural alteration was observed in 1,5 PDAN (Figure S14b and Figure S16). The significant improved stability of 1,5 PDAN can be attributed to strong π-π interaction between the polymer and carbon surface and within the polymer – a unique attribute of ladder polymers.[51] Further, the ladder structure of 1,5 PDAN should be less soluble in the electrolyte as opposed to the linear and less conjugated PANI.[52]
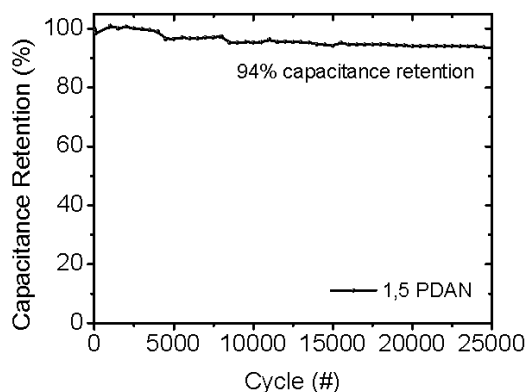
Figure 7. Cycle stability test for 1,5 PDAN on CNTs-a-CC for 25000 cycles at 100 mV/s scan rate.

1.5. Conclusions

We have developed a holistic method to conformally disperse redox species on the surface of the newly constructed carbon scaffold, CNTs-a-CC. This 3D scaffold, made of cylindrical micro- and nanostructures, offers well-defined and tunable micro- and nano-porous channels to facilitate ion and electron transport. Simultaneously, it offers excellent mechanical integrity allowing 1,5 PDAN conformal grafting to form a hierarchical nanostructure without altering the continuous porous architecture after polymer deposition.

Precise PDAN loading was achieved by the combination of charge flow analysis and weighing facilitated by the deposition of a thin layer of PDAN on CNTs-a-CC. This allows for accurate gravimetric capacitance estimation. Multiple sample characterization shows 1,5 PDAN possesses exceptionally high pseudocapacitance

between 900 F/g and 1250 F/g, which ranks among the best reported values of conductive polymers. The median 1100 F/g is only 20% less than the theoretical value for a polymer with 100% ladder structure, suggesting that a significant portion of a ladder structure present in the polymer system,

Owing to facile kinetics and unobstructed charge transport, an outstanding rate capability of 1250 F/g can be maintained up to 100 mV/s. Such a mechanically robust and open porous structure affords a significantly higher polymer loading. CNTs-a-CC allows for at least 10-fold more polymer loading than its flat or porous counterpart. 650 F/g at a loading of 2.5 mg/cm^2 has been attained with CNTs-a-CC. The reported facile fabrication method, monolithic integration of functional species with a 3D carbon without need of binder, enables electrochemical reactions in 3D. This approach can be used to fabricate electrodes for electrochemical sensing and possible electrocatalysis in 3D.

ASSOCIATED CONTENT

Supporting Information can be found in Appendix 1. Cu and Ni catalyst deposition; SEM images of Ni-Cu catalysts on a-CC surface; Amorphous carbon removal; Electro- oxidative polymerization via cyclic voltammetry in acidic medium; SEM image comparison with different polymerization cycles in acid; SEM image comparison with different polymerization cycles in acetonitrile; FTIR analysis of 1,5 PDAN; Weighted mass versus calculated mass in acetonitrile, CV analysis of 1,5 PDAN (20 pulses) on various substrates; SEM images of 1,5 PDAN on a-CC; Galvanostatic charge/discharge analysis; Nyquist plot; CV characteristics of PANI on a-CC; Stability test for PANI and PDAN; SEM images of PANI on a-CC before and after stability test; SEM images of PDAN before and after stability test.

Chapter 2: Metal-Nitrogen Coordinated Networks for ORR

Part 1: Investigation of Ligands and Oxidation State on Coordination Chemistry

2.1. Introduction

Pyridine is a heterocyclic aromatic organic molecule that closely resembles benzene; its only difference is that nitrogen replaces one of the carbons in the six membered ring[76]. The presence of the nitrogen hinders the resonance of the molecule. The lone pair in the pyridinic nitrogen does not participate in the aromaticity of pyridine, rather it sits outside the ring. Due to this pyridine behaves as a Lewis base as it can donate electrons to Lewis acids. Hence, the nitrogen in pyridine is able to participate in coordination bonds with metal ions, which are Lewis acids. The lone pair of electrons in the pyridinic nitrogen interacts with the empty d-orbitals of metal ions (scheme 2.1a). Pyridine causes a large slitting of the orbitals which allows for a strong metal-ligand bond. And as such it is classified as a relatively strong field ligand in crystal field theory[77].

 We can take advantage of the ability of pyridine to form coordination bonds with metals species that offer empty d-orbital to generate metal coordinated pyridine compounds. We conjecture that, after pyrolysis, this compound can turn into metal coordinated nitrogen doped carbon networks for electrocatalysts. In this work, poly(4- vinylpyridine), referred to as P4VP from now on, was used to create such a network. Typically, P4VP is a linear polymer, however it crosslinks with metal ions via complexation (scheme 2.1b). Pyrolyzing this metal complexed P4VP will yield a nitrogen rich carbon network for electrocatalysts. Metal precursors can have different oxidation states, orbital occupancy, and ligands and as a result it can impact the coordination chemistry. The goal of this work is to have comprehensive understanding on the effect different ligands have on the chemistry and yield N- doped carbon.
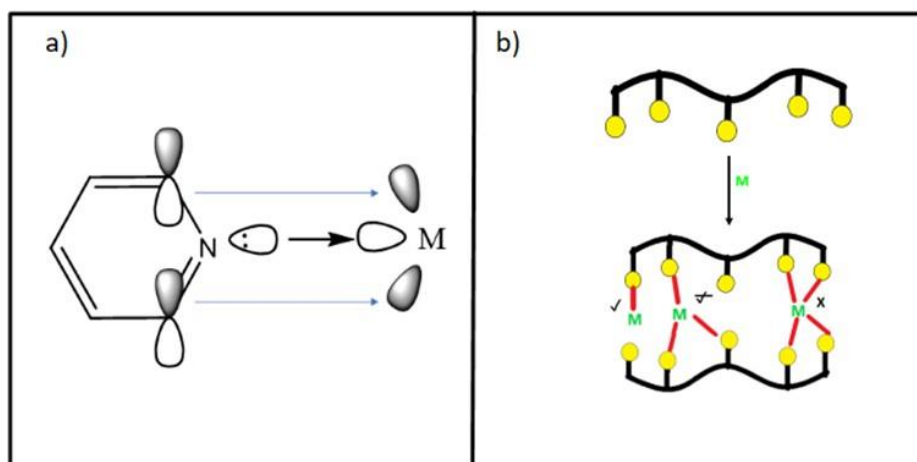
Scheme 2.1. (a) Pyridine and metal interaction. **(b)** Linear P4VP to crosslinked P4VP via complexation.

2.2. Experimental Methods

2.2.1. Tin Chloride (Sn(II)Cl and Sn(IV)Cl) and Tin Acetylacetonate (Sn(II)AcAc)

Poly(4-Vinylpyridine), P4VP, of Mw of 160,000 g/mol (n = 1522), tin (II) chloride, tin (IV) chloride, and tin(II) acetylacetonate were purchased from Sigma-Aldrich without purification. P4V4 was first dissolved in ethanol to make a 3 w/v% solution. The tin
(II) acetylacetonate, tin (II) and tin (IV) chlorides were dissolved in 5 mL of ethanol respectively. To form metal complexes P4VP with a molar ratio of metal:4VP of 2:1. First, 3 mL P4VP was added dropwise into a 5 mL ethanol solution that contains excess metal salt. White precipitate was immediately observed (Figure 2.1b-c). This is an indicator of successful the formation of Sn coordinated P4VP complexation.
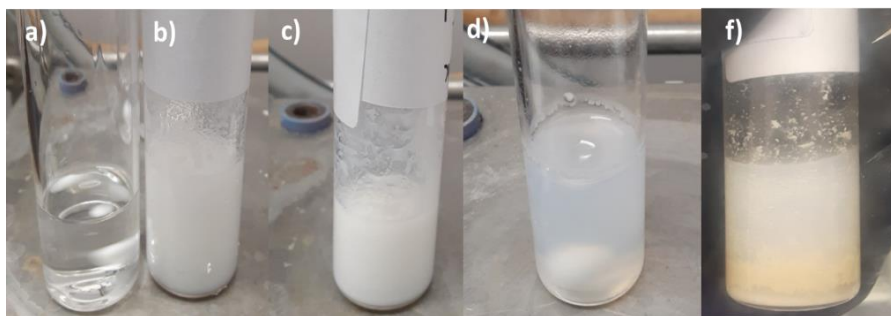
Figure 2.1. (a) P4VP in ethanol. **(b)** Sn(II)Cl-P4VP. **(c)** Sn(IV)Cl-P4VP. **(d)** Sn(IV)OAc-P4VP. **(f)** Sn(II)OAc-P4VP

To extract the white precipitates – product, the solution was transferred to a centrifuge tube and more ethanol was added to dissolve uncomplexed P4VP and excess metal salt. The precipitate was dispersed in ethanol. After mechanical stir and decantation of the solution. The entire process was repeated two times to ensure that the excess metal and uncomplexed polymer were removed.

2.2.2. Tin Acetate (Sn(II)OAc and Sn(IV)OAc)

For the Tin (II) acetate and Tin (IV) acetate salts ethanol could not be used as a solvent, instead acetone was used as the solvent for these solutions. However, acetone is not a good solvent for high molecular weight P4VP. So, to ensure that there was an interaction between the tin acetate salts and P4PV it was first determined how much acetone needed to be added to a 3 mL 3% wt/vol solution of P4VP without the polymer crashing the solution. From this small experiment of addition of acetone to a 3 mL 3% wt/vol solution of P4VP in ethanol it was concluded that 30 mL of acetone could be added before the polymer began to crash out (1:10 Ethanol: acetone ratio). Just like before 3 mL of P4VP solution was added to the metal solution. Upon addition of the P4VP to the tin (II) acetate solution there was a light cream precipitate while the tin (IV) complexation solution formed a white suspension (figure 2.1 d-f)

Table 1- Solubility of P4VP and various metal precursors in ethanol and acetone

Material	Ethanol Solubility	Acetone Solubility
P4VP	Soluble	Soluble for low molecular weight
Sn(II)Cl	Soluble	-
Sn(IV)Cl	Soluble	-
Sn(II)OAc	Not soluble	Partial suspension
Sn(II)AcAc	Soluble	-

2.3. Characterization

The resulting metal complexed polymer was characterized via Fourier-Transform Infrared (FTIR) spectroscopy with a Bruker Vertex 70 spectrometer. This characterization technique was employed to check for the presence of the coordination bond between the pyridinic nitrogen in P4VP and the metal precursors. Thermogravimetric analysis (TGA) was performed with an SDT-Q600 instrument to examine thermal stability of a metal coordinated polymer. From the degradation temperature and profile, the degree of crosslinking will be determined.

2.4. Results and Discussion

2.4.1. FTIR

After thorough rinse to remove unreacted P4VP and metal precursor, FTIR was used to confirm the presence of the coordination bond between P4VP and metal, using Sn with different types of ligands. The corresponding 1800 to 1300 cm^{-1} range is displayed Figure 2.2. First, we must note that P4VP has five distinctive peaks in this region. The peak at 1596 cm^{-1} corresponds to the C=N bond in the pyridine ring while the 1556, 1493, 1449 and 1413 cm^{-1} correspond to the characteristic vibrations of the pyridine ring itself. The C=N peak at 1596 cm^{-1} will help determine a successful complexation.

Figure 2.2 shows the effect different ligands have on complexation which can lead to crosslinking of P4VP. Sn (II)OAc has the highest degree of crosslinking as the FTIR peaks, especially the C=N peak, get widened out and they become less defined. Next Sn (IV)OAc and Sn (II)AcAc have a similar degree of crosslinking. Unlike acetate and acetylacetonate ligands, the Sn(II)Cl precursor has the lowest degree of crosslinking.

Sn(II)Cl and Sn(IV)Cl have two additional well-defined peaks with a blue shift. This indicates a strong interaction by shortening the bonds between metal and pyridine ring. The blue shift is an indication that the C=N bond was strengthened, and the bond length got shortened [80-82]. The larger the shift observed, the stronger the interaction is[80-82]. Comparing Sn(II)Cl with Sn(IV)Cl, we observe that after complexation the degree of strength of C=N is the same, but the intensity of the peak is different. A more intense peak is indicative of more Sn incorporation onto the pyridine ring.

TGA results shown in figure 2.3 corroborates with the Sn(II)OAc is the most crosslinked, followed by Sn(IV)OAc, Sn(II)AcAc, Sn(II)Cl and lastly by Sn(IV)Cl. Tin chloride salts have a much lower char yield than those of tin acetate and tin acetylacetonate coordinated P4VP.
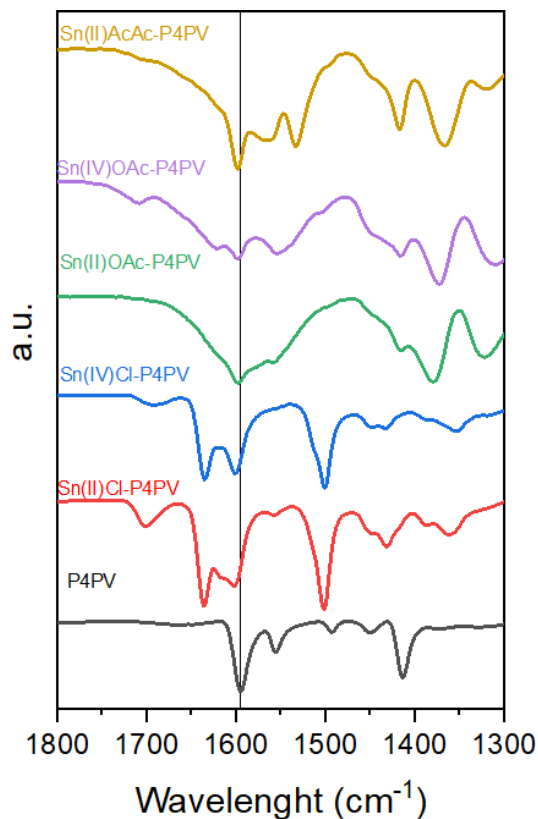
Figure 2.2. FTIR of P4VP and P4VP complexed with various metal salts.

2.4.2. TGA

TGA was used to look at the thermal stability and assess the successful completion of complexation. In figure 2.3 we observe the thermal degradation of P4VP and P4VP complexed with various metal salts. P4VP has a sharp degradation at 300 ^{o}C and the polymer is virtually gone by 450 ^{o}C. On the other hand, for metal crosslinked P4VP we can observe an earlier degradation of complexed P4VP than P4VP at about 200 ^{o}C. This is attributed to the metal interaction with the pyridine ring. The metal species allow for a better distribution of the electronic density of the ring. This causes a weaker interaction with the polymer backbone chain and hence an earlier degradation is seen below 200 ^{o}C. It can be seen that Sn (II)OAc has the highest

overall char yield (73.56%) followed by Sn(II)AcAc (56.64%), Sn(IV)OAc (53.63%), Sn(II)Cl (15.70%) and lastly by Sn(IV)Cl (14.23%). The char yield of the P4VP coordinated with tin acetate salts and tin acetylacetonate salt indicates a high degree of crosslinking due to complexation, just as predicted by FTIR. Finally, FTIR showed that the tin chloride salts had a high degree of complexation but not of crosslinking which is confirmed with the low char yield of said salts.
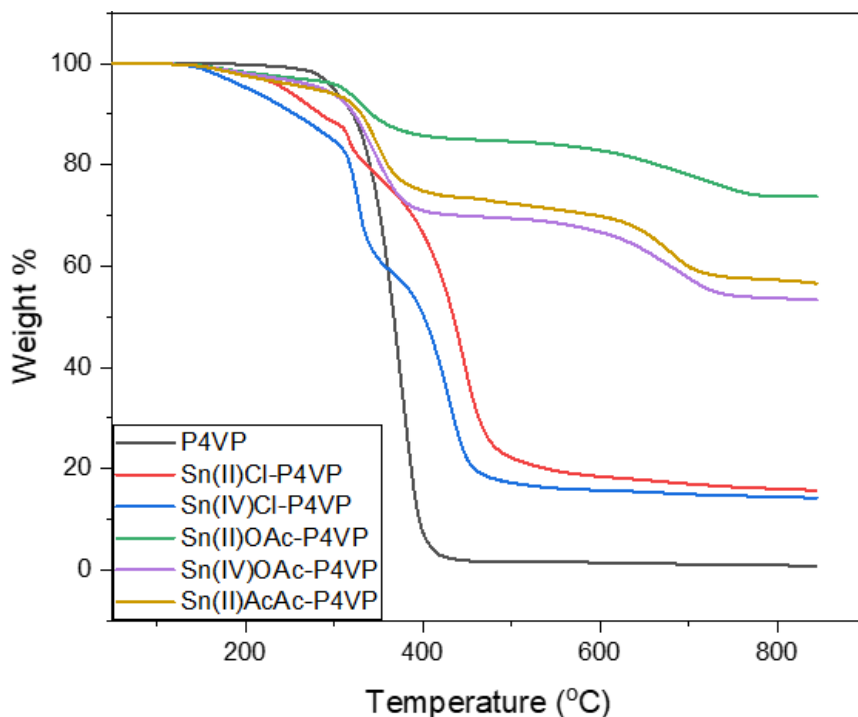
Figure 2.3. TGA curves of P4VP and P4VP complexed with various metal salts.

2.5. Conclusions

In this first part of the project, it was determined that the ligand of the metal precursor used to complex and crosslink the linear P4VP has an effect. From FTIR data we determined that bulky ligands like acetates and acetylacetonate allow for a high degree of crosslinking. On the other hand, chloride ligands allow for a high degree of complexation but not of crosslinking. This was further corroborated with TGA data. The TGA plots and char yields observed that the Sn (II)OAc had the highest overall char yield followed by the Sn (II)AcAc and lastly with the lowest overall char yield was the Sn (II)Cl and Sn(IV)Cl metal precursors. The data collected in this first part of the project will be further used to evaluate the ORR catalytic activity of catalysts made from precursors with different ligands.

Part 2: ORR Catalytic Investigation

2.6. Introduction

Polymer electrolyte membrane (PEM) based fuel cells produce electricity by consuming oxygen and hydrogen (Scheme 2.2). The only byproduct is water. This technology is one of vital green energy solutions[84]. However, the sluggish oxygen reduction reaction (ORR) is one of the bottlenecks to prevent commercialization. Often Platinum (Pt) is used to promote ORR. Not only a considerable amount of Pt needs to be used but Pt leaching and aggregation over time, limit the device cycle performance[85-87]. An alternative to Pt catalysts are non-precious metal coordinated nitrogen doped carbon catalysts (M-Nx-C)[88-92]. Over the past years there has been a great effort to generate and test these M-Nx-C catalysts. These catalysts are usually synthesized with the help of nitrogen rich precursors, carbon sources and non- precious metals such as Cobalt or Iron[88-93]. Said catalysts are very close to matching the performance of platinum catalysts. Taking inspiration from the literature and the first part of this chapter M-Nx-C catalysts were synthesized with the use of P4VP.

For the second part of this chapter the goal was to investigate the ORR catalytic activity of catalysts made from Sn (II)Cl and Sn (II)OAc. These two metal precursors were chosen based on the results from TGA and FTIR from the first part of this chapter. In particular we wanted to determine the influence that the ligand of the metal precursor had on the catalyst ORR activity. In addition to the tin precursors iron (II) chloride, cobalt (II) chloride and an alloy was evaluated to formulate the best catalysts possible. To test this cyclic voltammetry (CV) was employed to check the ORR catalytic activity. XPS was also used to check for nitrogen content of the catalysts synthesized with different ligands. Finally, some OER was also evaluated with the help of linear sweep voltammetry (LSV). The results from these tests are outlined in the next sections.
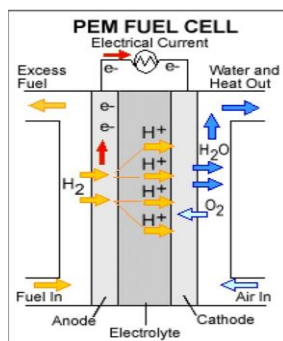
Hydrogen Oxidation Reaction

Anode: $2H_2 \rightarrow 4e + 4H^+$
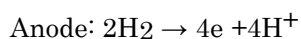
Hydrogen gets oxidized (0 to +1) and gives up electrons which travel from the anode to the cathode.

Oxygen Reduction Reaction

At cathode: $O_2 + H^+ + 4e \rightarrow 2H_2O$
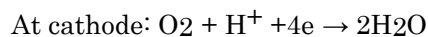
Protons travel through a polymer electrolyte membrane and react with oxygen to generate water. In this case, oxygen was reduced (-2 to 0)

Scheme 2.2. Fuel cell schematic adapted from Wikipedia[94]. This scheme describes the relevant redox reactions present at the anode and cathode of the PEM fuel cell.

2.7. Experimental Methods

2.7.1. Electrografting of P4VP onto Carbon Substrate

P4VP was electrografted onto a carbon substrate via reductive polymerization. To achieve this the carbon substrate was submerged onto a solution of acetonitrile, 125 mM distilled 4VP monomer, 50 mM ammonium perchlorate and 20 mM MBA (all chemicals were purchased via sigma aldrich). The 4VP monomer was then polymerized by running 60 CV cycles from -1 V to 2.7 V vs Ag/Ag+ with a CHI potentiostat. After polymerization substrates were air dried and weighed to check mass loading.

In addition, another polymerization method was tested. The same steps described above were taken to elecrograft the polymer into a carbon substrate. The only difference is that for the second method the 4VP monomer was first complexed with the metal precursor and then allowed to polymerize.

2.7.2. Preparation of M-Nx-C catalysts

After P4VP was electrografted onto a carbon substrate the polymer was complexed. Complexation solutions were made by dissolving metal salts (tin(II) chloride, tin (II) acetate, iron (II) chloride and cobalt (II) chloride) in anhydrous ethanol with a concentration of 50 mM. The P4VP samples were then submerged into their respective metal salt solution and allowed to soak for an hour. After the hour had passed the substrates were taken out of solution and allowed to air dry before pyrolysis. Once complexed samples were placed on an alumina boat and loaded into a quartz tube. The samples were then heated under a nitrogen atmosphere to either 850 $^{\circ}$C or 925 $^{\circ}$C and held there for 3 hours. After pyrolysis samples were leached with 1 M sulfuric acid for a minimum of 8 hours at room temperature to leach out excess metals. After leaching the samples were then annealed under a hydrogen atmosphere for 20 minutes to remove harmful oxygen species.

2.8. Characterization

The catalysts were characterized via cyclic voltammetry for ORR[103,104]. Each catalyst was tested under a nitrogen and oxygen atmosphere in 0.1 M HClO$_4$ at 10 mV/s. A graphite rod was used as a counter electrode, a saturated calomel electrode (SCE) was used as a reference electrode and the catalyst deposited on the carbon substrate were used as the working electrode. Additionally, some samples were tested for OER with linear sweep voltammetry at 10 mV/s in 0.1 M KOH. The reference electrode for this test was a Hg/HgO reference electrode while the working and counter electrodes remained the same as for ORR testing.

2.9. Results and Discussion

2.9.1. Electropolymerization of P4VP

P4VP can be electrografted onto carbon substrates via cathodic polymerization. Scheme 2.3 shows the electrografting process. A cathodic potential is applied to the working electrode. As a result, a negative charge builds due to the presence of electrons in the surface of the electrode. This allows for the monomer units to graft to the surface of the electrode and for the formation of radical cations that form the dimers, trimers and so on until polymer chains are formed.
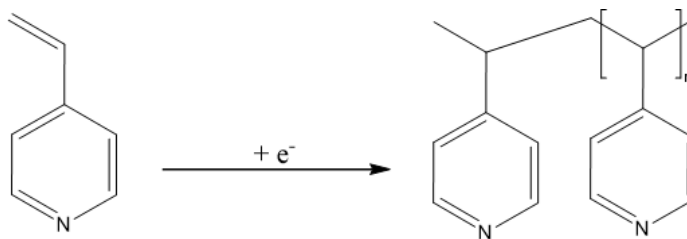
Scheme 2.3. Electropolymerization of P4VP.

2.9.2. Comparison of the synthesis method of M-Nx-C catalysts

In this work we tested two possible ways of forming the Sn-Nx-C catalysts. In the first method (denoted as soak) P4VP was electrografted onto a carbon substrate via cathodic polymerization first. The substrate was then soaked for an hour in a 50 mM solution made of ethanol and metal precursor. For the second method (denoted as M- 4VP where M stands for the metal used), The distilled monomer mixed with an excessive amount of metal precursor and poured onto the carbon substrate. Cathodic polymerization was then carried out. Both substrates were then annealed and treated as described in the experimental section. Figure 2.4 shows CV of ORR obtained from both polymerization methods. One can observe that the ORR catalytic activity of the catalysts synthesized from different methods is quite similar for both Co and Sn. The only difference that can be seen is that with the M-4VP method the surface area is much larger than the soak method. This is due to (1) excess metal and hence more char and (2) diffusion of the monomer solution onto carbon substrate. The ORR catalytic performance between two methods is comparable. This implies that either the composition of M-Nx-C derived from these two methods is the same or metal plays a more important role in determining the ORR catalytic activity of the M-Nx catalyst.
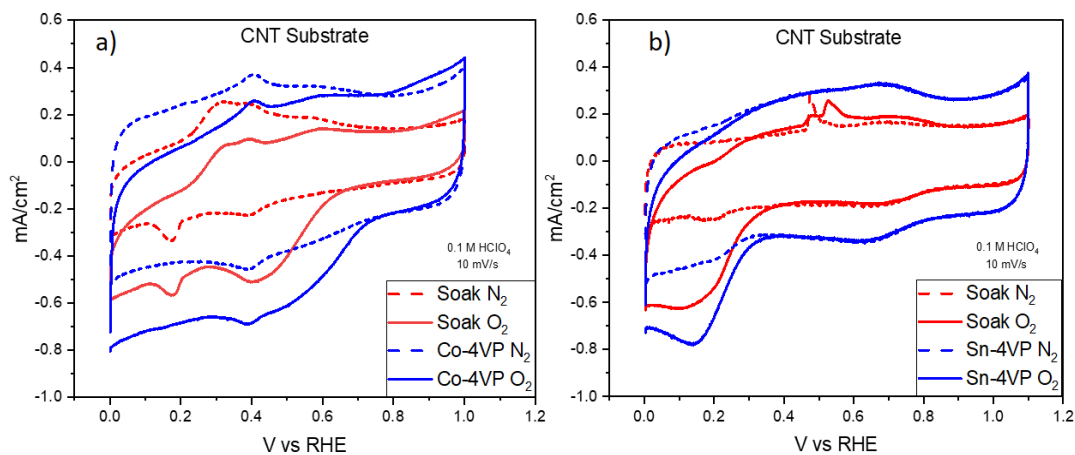
Figure 2.4. (a) CV curves under nitrogen and oxygen of Soak and Co-4VP synthesized catalysts in an acidic electrolyte at 10 mV/s. **(b)** CV curves under nitrogen and oxygen of Soak and Sn-4VP synthesized catalysts in an acidic electrolyte at 10 mV/s.

2.9.3. Effect of metal incorporation on char yield and effect on composition

To further confirm that the complexation of the P4VP samples was successful for the soak method one can look at the cyclic voltammetry results of samples after pyrolysis. In figure 2.5 we see the CV under a nitrogen atmosphere for P4VP, Sn(II)Cl-P4VP and Sn(II)OAc. It can be observed that the CV area of the pyrolyzed P4VP is smaller than that of Sn (II)Cl-P4VP and Sn (II)OAc, this indicates that the complexation was successful as a larger CV area is related to more material deposited on the surface of the substrate.
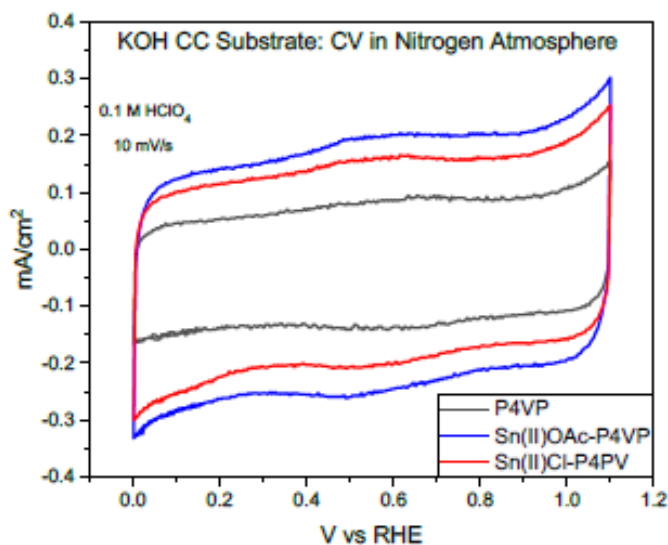
Figure 2.5. CV plots of P4VP, and complexed P4VP catalysts under nitrogen atmospheres at 10 mV/s in acidic electrolyte.

2.9.4. Effect of annealing temperature on ORR catalytic activity of Sn-N-C catalysts

Another parameter investigated in this study was the effect of annealing temperature on the resulting ORR activity. Nitrogen doped carbon plays an important role in the ORR activity of catalysts[95-97]. To generate this N-doped carbon samples are annealed at elevated temperatures under an inert atmosphere. To determine which annealing temperature would yield better ORR activity of samples complexed with Sn (II)Cl were annealed at 850 °C and °C 925 degrees. Figure 2.6 shows the CV under nitrogen and oxygen atmospheres. It can be seen that annealing at a higher temperature causes the CV area of nitrogen curves to be smaller which is expected as material will be removed at higher temperatures. It can also be seen that the onset potential for 925 °C is slightly better. The slope of 925 °C is steeper which implies a lower ORR activation barrier and higher ORR electrocatalytic activity[98,99]. Due to this, 925 °C was chosen as the annealing temperature for the formation of nitrogen doped carbon as well as the subsequent hydrogen treatment.
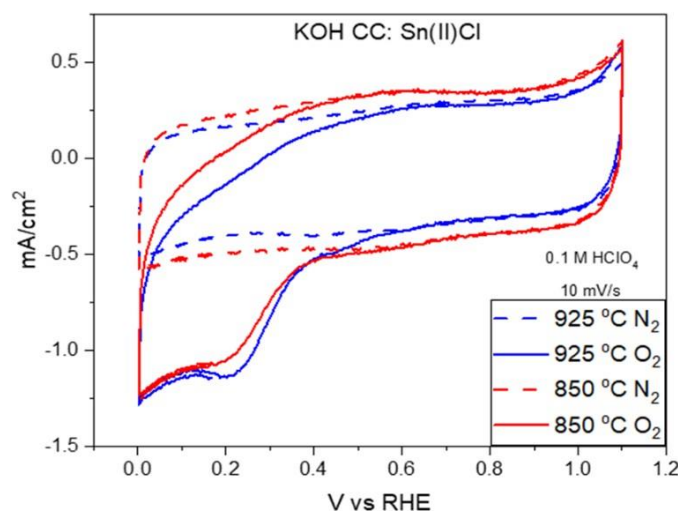
Figure 2.6. CV ORR catalytic activity of Sn catalysts synthesized at different temperatures in acidic electrolyte at 10 mV/s.

2.9.5 Effect of different ligands

In the first part of this chapter, it was determined that Sn (II)Cl and Sn (II)OAc metal precursors were going to be used to investigate the effect that a ligand may have in the ORR activity of the M-C-Nx catalysts. The stark results from the FTIR and TGA data in the first part of this chapter indicated that the coordination chemistry changed depending on the ligand on the metal precursor. This would mean that the ORR catalytic activity should have been impacted. However, as seen in figure 2.7a

the catalytic activities of Sn (II)Cl and Sn (II)OAc are remarkably similar. The one difference that can be seen in the CV data under a nitrogen atmosphere is that surface area of Sn (II)Cl is smaller than that of Sn (II)OAc. Indicating that Sn (II)OAc has more material in the surface of the electrode than Sn (II)Cl. This is further corroborated by XPS data in which it can be seen that the nitrogen content for Sn (II)OAc is higher than that of Sn (II)Cl (4.89% vs 3.48% respectively). This was expected because from the first part of this chapter we observed that Sn (II)OAc had a higher char yield, and hence retained more nitrogen and material, than Sn(II)Cl. So, from this we can conclude that the catalysts have a remarkably similar ORR catalytic activity, but Sn (II)Cl coordination chemistry can be more ORR active. We know this because Sn (II)Cl required less active material to have a similar ORR performance to that of Sn (II)OAc[77,100,105].
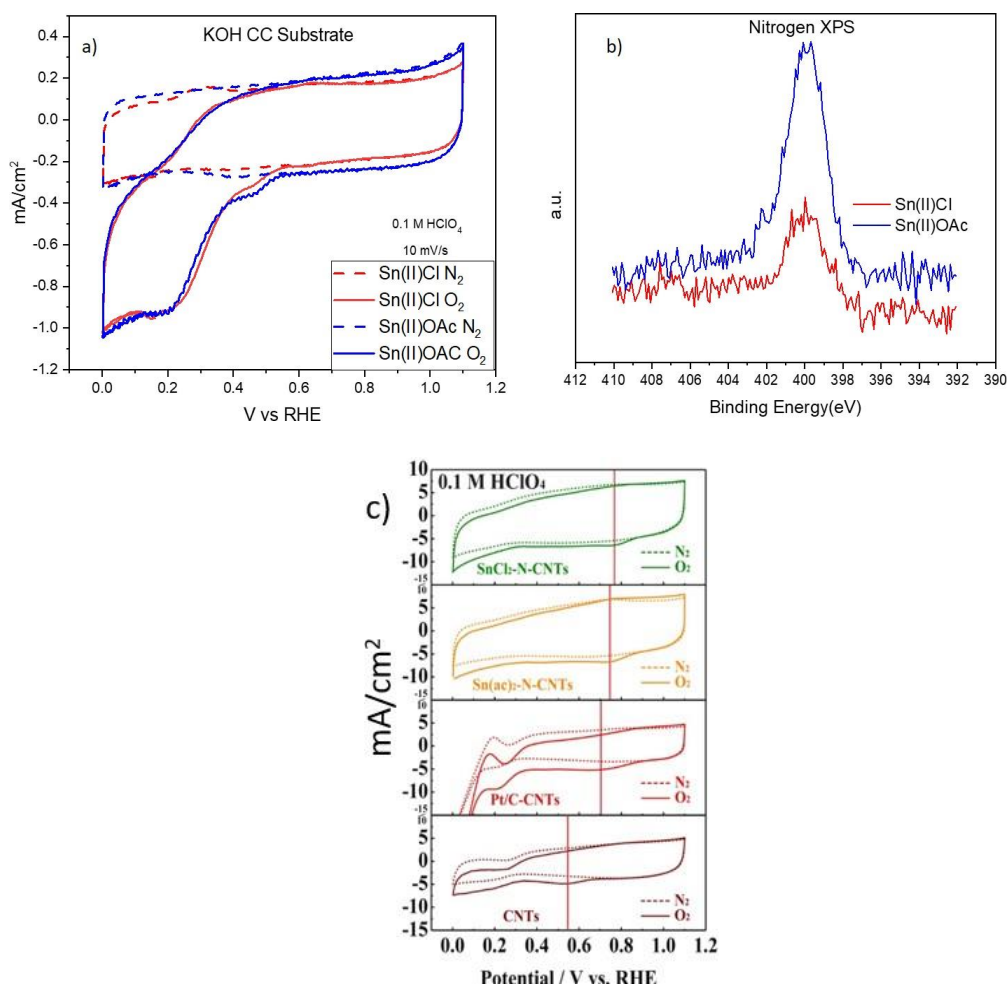
Figure 2.7. **(a)** CV of ORR catalytic activity of Sn catalysts synthesized with Sn(II)Cl and Sn(II)OAc in an acidic electrolyte at 10 mV/s. **(b)** Nitrogen XPS spectra for Sn(II)Cl and Sn(II)OAc catalysts. **(c)** CV of ORR catalytic of Sn catalysts synthesized with Sn(II)Cl and Sn(II)OAc, Pt catalyst and CNT substrate in an acidic electrolyte at 10 mV/s.

2.9.6. Effect of various metal precursors

Although for the majority of this project Tin metal salts were used to investigate ORR activity due to tin not undergoing the Fenton reaction[72]. It was easy to observe that tin did not have the best ORR catalytic activity. So, to find a better catalyst two additional metal precursors were tested, Co (II)Cl and Fe (II)Cl. These particular metal precursors were chosen as they had shown promising ORR catalytic activity in other systems. The Co and Fe catalysts were prepared in the same way as the Sn catalysts. In Figure 2.8 their electrochemical activity can be seen. Both Co and Fe catalysts outperform the Sn catalyst. The onset potential of the Co and Fe catalysts are 0.73 V and 0 .72 V vs RHE, respectively. These catalysts outperform even the best Sn catalyst (0.6 V vs RHE). Upon further inspection of the Co and Fe catalyst we observe that although they have very similar onset and half-way potentials ($E_{1/2}$=
0.63 V vs RHE for both catalysts) the ORR slope for the Co catalyst is much sharper and defined than the Fe one. This is an indication that the Co catalyst has better reaction kinetics than the Fe catalyst[97,98]. Another indication that Co is a better catalyst comes from the surface area of the catalysts under a nitrogen atmosphere. When looking at the CV surface area of the Fe and Co catalysts it was found that the surface area of the Fe catalyst was 1.4 times bigger than that of the Co catalyst. This indicates that although the Co catalyst has less active material than Fe, their catalytic activity was comparable[72,100,105], so Co was chosen as the best metal for ORR.
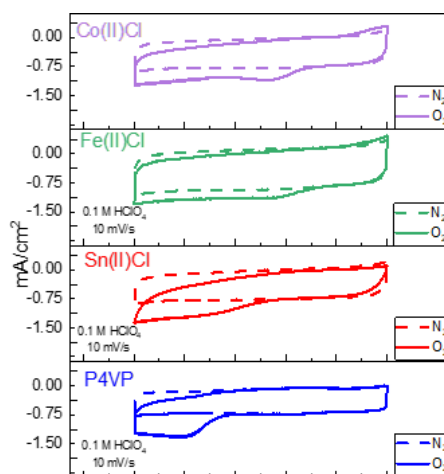
Figure 2.8. CV plots of carbon substrate, P4VP, and P4VP complexed with various metals under nitrogen and oxygen atmospheres at 10 mV/s in acidic electrolyte.

2.9.7. Cobalt/Tin catalyst ORR and OER

Because the cobalt catalyst performed so well it was decided that a composite of tin and cobalt should be used to see if the use of cobalt could boost the catalytic activity of tin. The composite was formed by mixing two 50 mM solutions of Co (II)Cl and Sn(II)Cl. The carbon substrate was then soaked for an hour in the solution and processed just like the catalysts in the previous sections of this chapter. Figure 2.9 shows the nitrogen and oxygen CV plots of pure cobalt and the Co:Sn composite. One can observe that the Co catalyst remains the best catalyst. However, with the Co:Sn composite we see that there is a small improvement in the onset and half-way potentials when compared to the pure Sn catalyst. The best performance for the Sn catalyst was an onset 0.6 V and an $E_{1/2}$= 0.43 V, for the Co:Sn composite the onset is 0.65 V and the $E_{1/2}$= 0.45 V. Alongside this we observed that the ORR slope for the composite is more defined and sharper than the pure Sn slope as seen in figure 2.9a This indicates that adding cobalt to the tin catalyst is useful to boost the ORR catalytic activity of tin[98,99]. Finally, we also tested to see if there was a similar effect of the addition of cobalt to the catalytic activity for OER. Figure 2.9b shows the OER plots for some cobalt composite. From the OER activity we see that the cobalt catalyst has the best OER activity with a 1.38 V vs RHE at 10 mA/cm^2. It can also be observed that the next best catalyst is the 2 Co:1 Sn catalyst followed by 1 Co: 2 Sn where the potentials at 10 mA/cm^2 are 1.58 V and 1.80 V respectively. Just like with ORR it can be seen that cobalt is a better catalyst for OER. Which indicates that the properties of cobalt are great for the energy conversion field. For future research one can make more cobalt catalyst and combine them with other transition metals such as zinc to try and tune the chemistry to find the best catalyst.
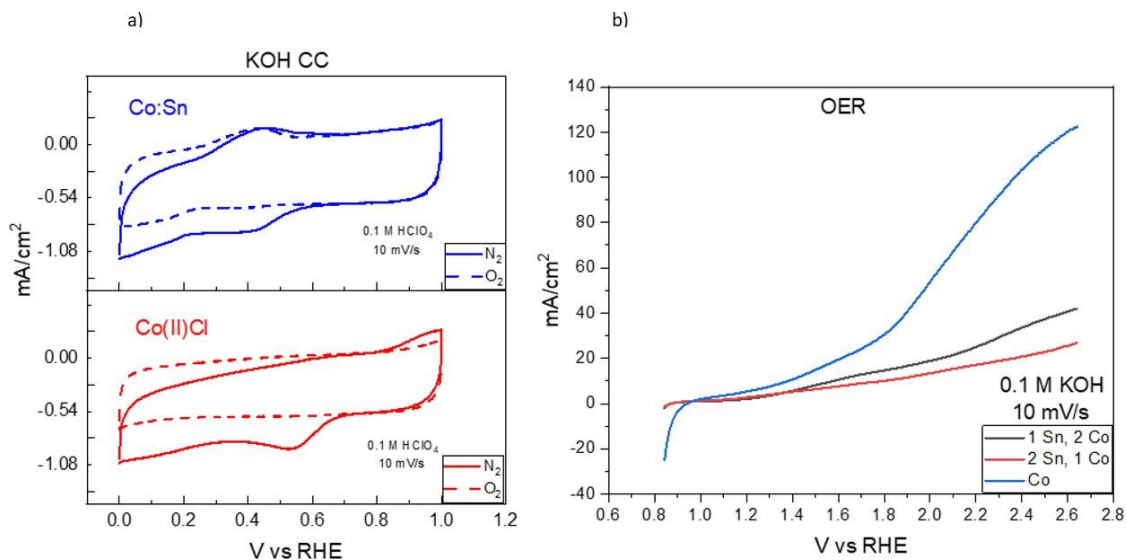
Figure 2.9. (a) CV of ORR catalytic activity of cobalt and Co:Sn composite in acidic electrolyte at 10 mV/s. **(b)** LSV of OER activity cobalt and Co:Sn composite in basic electrolyte at 10 mV/s.

2.9.8. CO₂ reduction and HER activity for Cu(II)Cl-P4VP

Finally, a test for the for CO$_2$ reduction and hydrogen evolution reaction (HER) was done with a cu(II)Cl-P4VP catalyst and compared to a commercial copper sample. CO$_2$ reduction is important to produce fuels such as ethylene, formate and more[101]. While HER is a promising way to generate hydrogen gas[102]. This was done by testing at two different potentials (-0.9 V and -1.1 V vs RHE). At the potential of -0.9 V the Cu-P4VP catalyst showed a higher selectivity towards CO$_2$ reduction than to HER (48.36% vs 30.43% respectively). The commercial copper sample also showed the same trend at -0.9 V with 60.6% for CO$_2$ reduction and 26.92% towards the HER reaction. However, at the potential of -1.1 V we see higher selectivity towards HER with the Cu-P4VP catalyst (55.53%) than for the CO$_2$ reduction (15.72%). For the commercial Cu sample, we see that, once again, there is higher selectivity for CO$_2$ reduction (63.91%) than for HER (18.19%). It is worth noting that for the Cu-P4VP there is a higher selectivity for HER than for commercial copper sample. This is an indication that Cu-P4VP catalyst can be used for HER applications, and if further tunned it may be a potential CO$_2$ reduction candidate.

2.10. Conclusions

In this work we determined the best way to synthesize a M-Nx-C catalyst. Two methods were compared: the soak method and the M-4VP method. Ultimately the soak method was chosen. Because it had comparable ORR catalytic activity to the M- 4VP method with the advantage of having less catalyst deposited in the surface of the carbon substrate. Afterwards we also determined the best annealing temperature for the best ORR activity which happened to be 925 ^{O}C. Once the synthesis and annealing temperature parameters were chosen, we compared Sn catalysts synthesized with metal precursors that contained different ligands. It was observed that the catalysts had comparable ORR catalytic activity. However, the catalyst that had chloride ions as ligands was able to offer the same ORR activity with less amount of catalyst deposited on the surface of the carbon substrate. Because of this the metal precursor with chloride ions as ligands was chosen to further synthesize M-Nx-C catalysts with iron, cobalt, copper, as well as composites of Co:Sn. By doing this we determined that cobalt containing catalysts were the best for ORR. Co was better because it had a more defined and steeper ORR slope than Fe containing catalysts and it outperformed Sn containing catalysts by a lot. We also observed that Co catalysts were good for OER, and the greater the amount of Co the better the performance. Finally, it was shown that our catalyst platform with copper as the metal source has promising results for HER. This shows how flexible this catalyst system can be. It is my hope that the findings in this work can be further utilized in the future. This catalyst platform has the opportunity to be refined to achieve greater performance for both ORR and OER and HER. By further tuning the coordination chemistry, as well as continuing to test other transition metals and treatments, such as ammonia treatments, the values reported here can be further improved. This catalyst platform can be of great use for ORR, OER and other catalytic applications.

REFERENCES

(1)   Jost, K.; Dion, G.; Gogotsi, Y. Textile Energy Storage in Perspective. *J. Mater. Chem. A* **2014**, *2* (28), 10776. https://doi.org/10.1039/c4ta00203b.

(2)   Park, H.; Kim, J. W.; Hong, S. Y.; Lee, G.; Lee, H.; Song, C.; Keum, K.; Jeong, Y. R.; Jin, S. W.; Kim, D. S.; Ha, J. S. Dynamically Stretchable Supercapacitor for Powering an Integrated Biosensor in an All-in-One Textile System. *ACS Nano* **2019**, *13* (9), 10469–10480. https://doi.org/10.1021/acsnano.9b04340.

(3)   Jost, K.; Perez, C. R.; McDonough, J. K.; Presser, V.; Heon, M.; Dion, G.; Gogotsi, Y. Carbon Coated Textiles for Flexible Energy Storage. *Energy Environ. Sci.* **2011**, *4* (12), 5060. https://doi.org/10.1039/c1ee02421c.

(4)   Ray, T. R.; Choi, J.; Bandodkar, A. J.; Krishnan, S.; Gutruf, P.; Tian, L.; Ghaffari, R.; Rogers, J. A. Bio-Integrated Wearable Systems: A Comprehensive Review. *Chem. Rev.* **2019**, *119* (8), 5461–5533. https://doi.org/10.1021/acs.chemrev.8b00573.

(5)   Yao, S.; Ren, P.; Song, R.; Liu, Y.; Huang, Q.; Dong, J.; O'Connor, B. T.; Zhu, Y. Nanomaterial-Enabled Flexible and Stretchable Sensing Systems: Processing, Integration, and Applications. *Adv. Mater.* **2020**, *32* (15), 1902343. https://doi.org/10.1002/adma.201902343.

(6)   Kenry; Yeo, J. C.; Lim, C. T. Emerging Flexible and Wearable Physical Sensing Platforms for Healthcare and Biomedical Applications. *Microsyst. Nanoeng.* **2016**, *2* (1), 16043. https://doi.org/10.1038/micronano.2016.43.

(7)   Kenan Döşoğlu, M.; Arsoy, A. B. Transient Modeling and Analysis of a DFIG Based Wind Farm with Supercapacitor Energy Storage. *Int. J. Electr. Power Energy Syst.* **2016**, *78*, 414–421. https://doi.org/10.1016/j.ijepes.2015.12.020.

(8)   Roth, E. P.; Orendorff, C. J. How Electrolytes Influence Battery Safety. *Interface Mag.* **2012**, *21* (2), 45–49. https://doi.org/10.1149/2.F04122if.

(9)   Ping, P.; Wang, Q.; Huang, P.; Li, K.; Sun, J.; Kong, D.; Chen, C. Study of the Fire Behavior of High-Energy Lithium-Ion Batteries with Full-Scale Burning Test. *J. Power Sources* **2015**, *285*, 80–89. https://doi.org/10.1016/j.jpowsour.2015.03.035.

(10)   Simon, P.; Gogotsi, Y. Materials for Electrochemical Capacitors. In *Nanoscience and Technology*; Co-Published with Macmillan Publishers Ltd, UK, 2009; pp 320–329. https://doi.org/10.1142/9789814287005_0033.

(11)   Shi, Y.; Peng, L.; Ding, Y.; Zhao, Y.; Yu, G. Nanostructured Conductive Polymers for Advanced Energy Storage. *Chem. Soc. Rev.* **2015**, *44* (19), 6684–6696. https://doi.org/10.1039/C5CS00362H.

(12)   Meng, Q.; Cai, K.; Chen, Y.; Chen, L. Research Progress on Conducting Polymer Based Supercapacitor Electrode Materials. *Nano Energy* **2017**, *36*, 268– 285. https://doi.org/10.1016/j.nanoen.2017.04.040.

(13)   Eftekhari, A.; Li, L.; Yang, Y. Polyaniline Supercapacitors. *J. Power Sources* **2017**, *347*, 86–107. https://doi.org/10.1016/j.jpowsour.2017.02.054.

(14)   Mike, J. F.; Lutkenhaus, J. L. Recent Advances in Conjugated Polymer Energy Storage. *J. Polym. Sci. Part B Polym. Phys.* **2013**, *51* (7), 468–480. https://doi.org/10.1002/polb.23256.

(15)   Bryan, A. M.; Santino, L. M.; Lu, Y.; Acharya, S.; D'Arcy, J. M. Conducting Polymers for Pseudocapacitive Energy Storage. *Chem. Mater.* **2016**, *28* (17), 5989– 5998. https://doi.org/10.1021/acs.chemmater.6b01762.

(16)   Zhang, Z.; Liao, M.; Lou, H.; Hu, Y.; Sun, X.; Peng, H. Conjugated Polymers for Flexible Energy Harvesting and Storage. *Adv. Mater.* **2018**, *30* (13), 1704261. https://doi.org/10.1002/adma.201704261.

(17)   Zhang, Q.; Zhou, A.; Wang, J.; Wu, J.; Bai, H. Degradation-Induced Capacitance: A New Insight into the Superior Capacitive Performance of Polyaniline/Graphene Composites. *Energy Environ. Sci.* **2017**, *10* (11), 2372–2382. https://doi.org/10.1039/C7EE02018J.

(18)   Liu, T.; Li, Y. Addressing the Achilles' Heel of Pseudocapacitive Materials: Long-term Stability. *InfoMat* **2020**, *2* (5), 807–842. https://doi.org/10.1002/inf2.12105.

(19)   Snook, G. A.; Kao, P.; Best, A. S. Conducting-Polymer-Based Supercapacitor Devices and Electrodes. *J. Power Sources* **2011**, *196* (1), 1–12. https://doi.org/10.1016/j.jpowsour.2010.06.084.

(20)   Kou, T.; Yao, B.; Liu, T.; Li, Y. Recent Advances in Chemical Methods for Activating Carbon and Metal Oxide Based Electrodes for Supercapacitors. *J Mater Chem A* **2017**, *5* (33), 17151–17173. https://doi.org/10.1039/C7TA05003H.

(21)   Li, H.; Wang, J.; Chu, Q.; Wang, Z.; Zhang, F.; Wang, S. Theoretical and Experimental Specific Capacitance of Polyaniline in Sulfuric Acid. *J. Power Sources* **2009**, *190* (2), 578–586. https://doi.org/10.1016/j.jpowsour.2009.01.052.

(22)   Oyama, N.; Sato, M.; Ohsaka, T. Preparation of Thin Polymeric Films on Electrode Surfaces by Electro-Polymerization of Aromatic Compounds with Amino Groups. *Synth. Met.* **1989**, *29* (1), 501–506. https://doi.org/10.1016/0379- 6779(89)90340-8.

(23)   Jackowska, K.; Bukowska, J.; Jamkowski, M. Synthesis, Electroactivity and Molecular Structure of Poly(1,5-Diaminonaphthalene). *J. Electroanal. Chem.* **1995**, *388* (1–2), 101–108. https://doi.org/10.1016/0022-0728(95)03912-Z.

(24)   Skompska, M.; Hillman, A. R. Electrochemical Quartz Crystal Microbalance Studies of the Electropolymerization, Electroactivity and Complexing Properties of Poly(1,8-Diaminonaphthalene) Films. *J. Chem. Soc. Faraday Trans.* **1996**, *92* (20), 4101. https://doi.org/10.1039/ft9969204101.

(25)   Li, X.-G.; Huang, M.-R.; Duan, W.; Yang, Y.-L. Novel Multifunctional Polymers from Aromatic Diamines by Oxidative Polymerizations. *Chem. Rev.* **2002**, *102* (9), 2925–3030. https://doi.org/10.1021/cr010423z.

(26)   Abdel Azzem, M.; Yousef, U. S.; Limosin, D.; Pierre, G. Electro-Oxidative Oligomerization of 1,5-Diaminonaphthalene in Acetonitrile Medium. *J. Electroanal. Chem.* **1996**, *417* (1–2), 163–173. https://doi.org/10.1016/S0022-0728(96)04729-8.

(27)   Hong, S.-Y.; Park, S.-M. Electrochemistry of Conductive Polymers. *J. Electrochem. Soc.* **2003**, *150* (7), E360. https://doi.org/10.1149/1.1580826.

(28)   Pham, M.-C.; Oulahyne, M.; Mostefai, M.; Chehimi, M. M. Multiple Internal Reflection FT-IR Spectroscopy (MIRFTIRS) Study of the Electrochemical Synthesis and Redox Process of Poly (1,5-Diaminonaphthalene). *Synth. Met.* **1998**, *93* (2), 89– 96. https://doi.org/10.1016/S0379-6779(97)03946-5.

(29)   Lee, J.; Kalin, A. J.; Yuan, T.; Al-Hashimi, M.; Fang, L. Fully Conjugated Ladder Polymers. *Chem. Sci.* **2017**, *8* (4), 2503–2521. https://doi.org/10.1039/C7SC00154A.

(30)   Wu, Y.; Zhang, J.; Fei, Z.; Bo, Z., Spiro-Bridged Ladder-Type Poly(p-phenylene)s: Towards Structurally Perfect Light-Emitting Materials. *J Am Chem Soc* **2008,** *130* (23), 7192-7193.

(31)   Santos, L. M.; Ghilane, J.; Fave, C.; Lacaze, P.-C.; Randriamahazaka, H.; Abrantes, L. M.; Lacroix, J.-C. Electrografting Polyaniline on Carbon through the Electroreduction of Diazonium Salts and the Electrochemical Polymerization of Aniline. *J. Phys. Chem. C* **2008**, *112* (41), 16103–16109. https://doi.org/10.1021/jp8042818.

(32)   Huang, Y.; Li, H.; Wang, Z.; Zhu, M.; Pei, Z.; Xue, Q.; Huang, Y.; Zhi, C. Nanostructured Polypyrrole as a Flexible Electrode Material of Supercapacitor. *Nano Energy* **2016**, *22*, 422–438. https://doi.org/10.1016/j.nanoen.2016.02.047.

(33)   Peng, C.; Hu, D.; Chen, G. Z. Theoretical Specific Capacitance Based on Charge Storage Mechanisms of Conducting Polymers: Comment on 'Vertically Oriented Arrays of Polyaniline Nanorods and Their Super Electrochemical Properties.' *Chem. Commun.* **2011**, *47* (14), 4105. https://doi.org/10.1039/c1cc10675a.

(34)   Hung, K.-H.; Tzeng, S.-S.; Kuo, W.-S.; Wei, B.; Ko, T.-H. Growth of Carbon Nanofibers on Carbon Fabric with Ni Nanocatalyst Prepared Using Pulse Electrodeposition. *Nanotechnology* **2008**, *19* (29), 295602. https://doi.org/10.1088/0957-4484/19/29/295602.

(35)   Pan, D.; Ombaba, M.; Zhou, Z.-Y.; Liu, Y.; Chen, S.; Lu, J. Direct Growth of Carbon Nanofibers to Generate a 3D Porous Platform on a Metal Contact to Enable an Oxygen Reduction Reaction. *ACS Nano* **2012**, *6* (12), 10720–10726. https://doi.org/10.1021/nn303910w.

(36)   Chen, C.-C.; Chen, C. F.; Hsu, C.-H.; Li, I.-H. Growth and Characteristics of Carbon Nanotubes on Carbon Cloth as Electrodes. *Diam. Relat. Mater.* **2005**, *14* (3– 7), 770–773. https://doi.org/10.1016/j.diamond.2004.12.038.

(37)   Cesano, F.; Bertarione, S.; Scarano, D.; Zecchina, A. Connecting Carbon Fibers by Means of Catalytically Grown Nanofilaments: Formation of Carbon−Carbon Composites. *Chem. Mater.* **2005**, *17* (20), 5119–5123. https://doi.org/10.1021/cm050427a.

(38)   Baker, R. T. K. Catalytic Growth of Carbon Filaments. *Carbon* **1989**, *27* (3), 315–323. https://doi.org/10.1016/0008-6223(89)90062-6.

(39)   Deck, C. P.; Vecchio, K. Prediction of Carbon Nanotube Growth Success by the Analysis of Carbon–Catalyst Binary Phase Diagrams. *Carbon* **2006**, *44* (2), 267–275. https://doi.org/10.1016/j.carbon.2005.07.023.

(40)   Zhou, W.; Han, Z.; Wang, J.; Zhang, Y.; Jin, Z.; Sun, X.; Zhang, Y.; Yan, C.; Li, Y. Copper Catalyzing Growth of Single-Walled Carbon Nanotubes on Substrates. *Nano Lett.* **2006**, *6* (12), 2987–2990. https://doi.org/10.1021/nl061871v.

(41)   Kukovitsky, E. F.; L'vov, S. G.; Sainov, N. A.; Shustov, V. A.; Chernozatonskii, L. A. Correlation between Metal Catalyst Particle Size and Carbon Nanotube Growth. *Chem. Phys. Lett.* **2002**, *355* (5–6), 497–503. https://doi.org/10.1016/S0009- 2614(02)00283-X.

(42)   Wang, J.; Kaskel, S. KOH Activation of Carbon-Based Materials for Energy Storage. *J. Mater. Chem.* **2012**, *22* (45), 23710. https://doi.org/10.1039/c2jm34066f.

(43)   Meneguzzi, A.; Pham, M. C.; Lacroix, J.-C.; Piro, B.; Adenier, A.; Ferreira, C. A.; Lacaze, P.-C. Electroactive Poly(Aromatic Amine) Films for Iron Protection in Sulfate Medium. *J. Electrochem. Soc.* **2001**, *148* (4), B121. https://doi.org/10.1149/1.1354613.

(44)   Nasalska, A.; Skompska, M. Removal of Toxic Chromate Ions by the Films of Poly(1,8-Diaminonaphthalene). *J. Appl. Electrochem.* **2003**, *33* (1), 113–119. https://doi.org/10.1023/A:1022952019530.

(45)   Duić, Lj.; Grigić, S. The Effect of Polyaniline Morphology on Hydroquinone/Quinone Redox Reaction. *Electrochimica Acta* **2001**, *46* (18), 2795– 2803. https://doi.org/10.1016/S0013-4686(01)00491-1.

(46)   Kiliç, R.; Hür, E.; Arslan, A. Poly(1,5-Diaminonaphthalene) Films for Supercapacitor Electrode Materials: Effect of Electropolymerization Technique on Specific Capacitance. *Chem. Pap.* **2017**, *71* (7), 1311–1321. https://doi.org/10.1007/s11696-016-0123-2.

(47)   Jackowska, K.; Skompska, M.; Przyłuska, E. Electro-Oxidation of 1,5 and 1,8 Diaminonaphthalene: An RDE Study. *J. Electroanal. Chem.* **1996**, *418* (1–2), 35–39. https://doi.org/10.1016/S0022-0728(96)04852-8.

(48)   Jin, C.-S.; Shim, Y.-B.; Park, S.-M. Electropolymerization and Spectroelectrochemical Characterization of Poly(1,5-Diaminonaphthalene). *Synth. Met.* **1995**, *69* (1–3), 561–562. https://doi.org/10.1016/0379-6779(94)02569-K.

(49)   Gogotsi, Y.; Penner, R. M. Energy Storage in Nanomaterials – Capacitive, Pseudocapacitive, or Battery-Like? *ACS Nano* **2018**, *12* (3), 2081–2083. https://doi.org/10.1021/acsnano.8b01914.

(50)   Yan, J.; Wei, T.; Fan, Z.; Qian, W.; Zhang, M.; Shen, X.; Wei, F. Preparation of Graphene Nanosheet/Carbon Nanotube/Polyaniline Composite as Electrode Material for Supercapacitors. *J. Power Sources* **2010**, *195* (9), 3041–3045. https://doi.org/10.1016/j.jpowsour.2009.11.028.

(51)   Abdel-Aziz, A. M.; Hassan, H. H.; Hassan, A. A.; Badr, I. H. A. A Sensitive and Green Method for Determination of Catechol Using Multi-Walled Carbon Nanotubes/Poly(1,5-Diaminonaphthalene) Composite Film Modified Glassy Carbon Electrode. *J. Electrochem. Soc.* **2019**, *166* (15), B1441–B1451. https://doi.org/10.1149/2.0301915jes.

(52)   Teo, Y. C.; Lai, H. W. H.; Xia, Y. Synthesis of Ladder Polymers: Developments, Challenges, and Opportunities. *Chem. – Eur. J.* **2017**, *23* (57), 14101–14112. https://doi.org/10.1002/chem.201702219.

(53)   *U.S. energy facts explained - consumption and production - U.S. Energy Information Administration (EIA)*. Eia.gov. (2022). Retrieved from https://www.eia.gov/energyexplained/us-energy-facts/.

(54)   Sommer, L., (2022). California just ran on 100% renewable energy, but fossil fuels aren't fading away yet. *NPR*. https://www.npr.org/2022/05/07/1097376890/for- a-brief-moment-calif-fully-powered-itself-with-renewable-energy

(55)   Chediak, M. (2022). California Ran on Nearly 100% Clean Energy This Month. *Bloomberg*. https://www.bloomberg.com/news/articles/2022-04-14/california- ran-on-nearly-100-clean-energy-this-month#xj4y7vzkg.

(56)   Miao, Y. E., & Liu, T. (2019). Electrospun nanofiber electrodes: A promising platform for supercapacitor applications. In *Electrospinning: Nanofabrication and Applications* (pp. 641-669). William Andrew Publishing.

(57)   Sarno, M. (2020). Nanotechnology in energy storage: The supercapacitors. In *Studies in Surface Science and Catalysis* (Vol. 179, pp. 431-458). Elsevier.

(58)   Ehsani, A., Heidari, A. A., & Shiri, H. M. (2019). Electrochemical pseudocapacitors based on ternary nanocomposite of conductive polymer/ graphene/ metal oxide: an introduction and review to it in recent studies. *The Chemical Record*, *19*(5), 908-926.

(59)   Cheng, C., & Ngan, A. H. (2015). Reversible electrochemical actuation of metallic nanohoneycombs induced by pseudocapacitive redox processes. *ACS nano*, *9*(4), 3984-3995.

(60)   Jiang, Y., & Liu, J. (2019). Definitions of pseudocapacitive materials: a brief review. *Energy & Environmental Materials*, *2*(1), 30-37.

(61)   Yi, C. Q., Zou, J. P., Yang, H. Z., & Xian, L. E. N. G. (2018). Recent advances in pseudocapacitor electrode materials: transition metal oxides and nitrides. *Transactions of Nonferrous Metals Society of China*, *28*(10), 1980-2001.

(62)   Suriyakumar, S., Bhardwaj, P., Grace, A. N., & Stephan, A. M. (2021). Role of polymers in enhancing the performance of electrochemical supercapacitors: a review. *Batteries & Supercaps*, *4*(4), 571-584.

(63)   Naskar, P., Maiti, A., Chakraborty, P., Kundu, D., Biswas, B., & Banerjee, A. (2021). Chemical supercapacitors: a review focusing on metallic compounds and conducting polymers. *Journal of Materials Chemistry A*, *9*(4), 1970-2017.

(64)   Chang, L., & Hang Hu, Y. (2018). 2.21 Supercapacitors. *Comprehensive Energy Systems*, 663-695.

(65)   Abdah, M. A. A. M., Azman, N. H. N., Kulandaivalu, S., & Sulaiman, Y. (2020). Review of the use of transition-metal-oxide and conducting polymer-based fibres for high-performance supercapacitors. *Materials & Design*, *186*, 108199.

(66)   Schoots, K., Kramer, G. J., & van der Zwaan, B. C. C. (2010). Technology learning for fuel cells: an assessment of past and potential cost reductions. *Energy policy*, *38*(6), 2887-2897.

(67)   Wang, Y., Diaz, D. F. R., Chen, K. S., Wang, Z., & Adroher, X. C. (2020). Materials, technological status, and fundamentals of PEM fuel cells–a review. *Materials today*, *32*, 178-203.

(68)   Felseghi, R. A., Carcadea, E., Raboaca, M. S., Trufin, C. N., & Filote, C. (2019). Hydrogen fuel cell technology for the sustainable future of stationary applications. *Energies*, *12*(23), 4593.

(69)   Zhao, D., Zhuang, Z., Cao, X., Zhang, C., Peng, Q., Chen, C., & Li, Y. (2020). Atomic site electrocatalysts for water splitting, oxygen reduction and selective oxidation. *Chemical Society Reviews*, *49*(7), 2215-2264.

(70)   Wang, J. (2017). System integration, durability and reliability of fuel cells: Challenges and solutions. *Applied Energy*, *189*, 460-479.

(71)   Wu, J., Pan, Z., Zhang, Y., Wang, B., & Peng, H. (2018). The recent progress of nitrogen-doped carbon nanomaterials for electrochemical batteries. *Journal of Materials Chemistry A*, *6*(27), 12932-12944.

(72)   Luo, F., Roy, A., Silvioli, L., Cullen, D. A., Zitolo, A., Sougrati, M. T., ... & Strasser, P. (2020). P-block single-metal-site tin/nitrogen-doped carbon fuel cell cathode catalyst for oxygen reduction reaction. *Nature Materials*, *19*(11), 1215-1223.

(73)   Gu, W., Hu, L., Li, J., & Wang, E. (2018). Recent Advancements in Transition Metal-Nitrogen-Carbon Catalysts for Oxygen Reduction Reaction. *Electroanalysis*, *30*(7), 1217-1228.

(74)   Zhu, Z., Yin, H., Wang, Y., Chuang, C. H., Xing, L., Dong, M., ... & Zhao, H. (2020). Coexisting single-atomic Fe and Ni sites on hierarchically ordered porous carbon as a highly efficient ORR electrocatalyst. *Advanced Materials*, *32*(42), 2004670.

(75)   Chen, Y., Gao, R., Ji, S., Li, H., Tang, K., Jiang, P., ... & Li, Y. (2021). Atomic- level modulation of electronic density at cobalt single-atom sites derived from metal–organic frameworks: enhanced oxygen reduction performance. *Angewandte Chemie International Edition*, *60*(6), 3212-3221.

(76)   Scriven, E. F., & Murugan, R. (2005). Pyridine and pyridine derivatives Kirk- Othmer Encyclopedia of Chemical Technology 4th edn, Vol 20 John Wiley &

Sons. *Inc: Hoboken, NJ*.

(77)   Pal, S. (2018). Pyridine: A useful ligand in transition metal complexes. *Pyridine* (edited by Pandey, P. P.) IntechOpen, 57-74.

(78)   Nose, H., & Rodgers, M. T. (2014). Influence of the d orbital occupation on the structures and sequential binding energies of pyridine to the late first-row divalent transition metal cations: a DFT study. *The Journal of Physical Chemistry A*, *118*(37), 8129-8140.

(79)   Kline Jr, C. H., & Turkevich, J. (1944). The vibrational spectrum of pyridine and the thermodynamic properties of pyridine vapors. *The Journal of Chemical Physics*, *12*(7), 300-309.

(80)   Santana, A. L., Noda, L. K., Pires, A. T. N., & Bertolino, J. R. (2004). Poly (4- vinylpyridine)/cupric salt complexes: Spectroscopic and thermal properties. *polymer testing*, *23*(7), 839-845.

(81)   Rodrigues, J. D. S., Goncalves, D., Mangrich, A. S., Soldi, V., Bertolino, J. R., & Pires, A. T. N. (2000). Thermal behavior and electrical conductivity of poly (vinyl pyridine)/copper complexes. *Advances in Polymer Technology: Journal of the Polymer Processing Institute*, *19*(2), 113-119.

(82)   Wu, K. H., Wang, Y. R., & Hwu, W. H. (2003). FTIR and TGA studies of poly (4-vinylpyridine-co-divinylbenzene)–Cu (II) complex. *Polymer degradation and stability*, *79*(2), 195-200.

(83)   Akçay, M. (2005). The surface acidity and characterization of Fe-montmorillonite probed by in situ FT-IR spectroscopy of adsorbed pyridine. *Applied Catalysis A: General*, *294*(2), 156-160.

(84)   Abdelkareem, M. A., Elsaid, K., Wilberforce, T., Kamil, M., Sayed, E. T., & Olabi, A. (2021). Environmental aspects of fuel cells: A review. *Science of The Total Environment*, *752*, 141803.

(85)   Ren, X., Lv, Q., Liu, L., Liu, B., Wang, Y., Liu, A., & Wu, G. (2020). Current progress of Pt and Pt-based electrocatalysts used for fuel cells. *Sustainable Energy & Fuels*, *4*(1), 15-30.

(86)   Li, D., Wang, C., Strmcnik, D. S., Tripkovic, D. V., Sun, X., Kang, Y., ... & Markovic, N. M. (2014). Functional links between Pt single crystal morphology and nanoparticles with different size and shape: the oxygen reduction reaction case. *Energy & Environmental Science*, *7*(12), 4061-4069.

(87)   Wu, D., Shen, X., Pan, Y., Yao, L., & Peng, Z. (2020). Platinum alloy catalysts for oxygen reduction reaction: Advances, challenges and perspectives. *ChemNanoMat*, *6*(1), 32-41.

(88)   Zhao, W., Ye, Y., Jiang, W., Li, J., Tang, H., Hu, J., ... & Liao, S. (2020). Mesoporous carbon confined intermetallic nanoparticles as highly durable electrocatalysts for the oxygen reduction reaction. *Journal of Materials Chemistry A*, *8*(31), 15822-15828.

(89)   Chen, M. X., Zhu, M., Zuo, M., Chu, S. Q., Zhang, J., Wu, Y., ... & Feng, X. (2020). Identification of catalytic sites for oxygen reduction in metal/nitrogen-doped carbons with encapsulated metal nanoparticles. *Angewandte Chemie*, *132*(4), 1644- 1650.

(90)   Zang, J., Wang, F., Cheng, Q., Wang, G., Ma, L., Chen, C., ... & Yang, H. (2020). Cobalt/zinc dual-sites coordinated with nitrogen in nanofibers enabling efficient and durable oxygen reduction reaction in acidic fuel cells. *Journal of Materials Chemistry A*, *8*(7), 3686-3691.

(91)   Yin, S. H., Yang, J., Han, Y., Li, G., Wan, L. Y., Chen, Y. H., ... & Sun, S. G. (2020). Construction of highly active metal-containing nanoparticles and FeCo-N4 composite sites for the acidic oxygen reduction reaction. *Angewandte Chemie*, *132*(49), 22160-22163.

(92)   He, Y., Tan, Q., Lu, L., Sokolowski, J., & Wu, G. (2019). Metal-nitrogen-carbon catalysts for oxygen reduction in PEM fuel cells: self-template synthesis approach to enhancing catalytic activity and stability. *Electrochemical Energy Reviews*, *2*(2), 231-251.

(93)   Du, L., Zhang, G., Liu, X., Hassanpour, A., Dubois, M., Tavares, A. C., & Sun, S. (2020). Biomass-derived nonprecious metal catalysts for oxygen reduction reaction: The demand-oriented engineering of active sites and structures. *Carbon Energy*, *2*(4), 561-581.

(94)   Wikimedia Foundation. (2022, May 19). *Fuel cell*. Wikipedia. Retrieved 2022, from https://en.wikipedia.org/wiki/Fuel_cell#/media/File:Solid_oxide_fuel_cell_protonic.svg

(95)   Gokuladeepan, P., & Karthigeyan, A. (2018). Effect of annealing temperature on oxygen reduction reaction of reduced graphene oxide incorporated cobalt oxide nanocomposites for fuel cell applications. *Applied Surface Science*, *449*, 705-711.

(96)   Samad, S., Loh, K. S., Wong, W. Y., Sudarsono, W., Lee, T. K., & Daud, W. R. W. (2020). Effect of various Fe/Co ratios and annealing temperatures on a Fe/Co

catalyst supported with nitrogen-doped reduced graphene oxide towards the oxygen reduction reaction. *Journal of Alloys and Compounds*, *816*, 152573.

(97)   Zhao, Y., Zhang, L., Wei, W., Li, Y., Liu, A., Zhang, Y., & Liu, S. (2015). Effect of annealing temperature and element composition of titanium dioxide / graphene / hemin catalysts for oxygen reduction reaction. *RSC advances*, *5*(101), 82879-82886.

(98)   Park, Y., Lee, B., Kim, C., Kim, J., Nam, S., Oh, Y., & Park, B. (2010). Modification of gold catalysis with aluminum phosphate for oxygen-reduction reaction. *The Journal of Physical Chemistry C*, *114*(8), 3688-3692.

(99)   Gadipelli, S., Zhao, T., Shevlin, S. A., & Guo, Z. (2016). Switching effective oxygen reduction and evolution performance by controlled graphitization of a cobalt–nitrogen–carbon framework system. *Energy & Environmental Science*, *9*(5),   1661-1667.

(100)   Zhuang, Z., & Chen, W. (2019). Ultra-low loading of Pd5 nanoclusters on carbon nanotubes as bifunctional electrocatalysts for the oxygen reduction reaction and the ethanol oxidation reaction. *Journal of colloid and interface science*, *538*, 699-708.

(101)   Yu, J., Wang, J., Ma, Y., Zhou, J., Wang, Y., Lu, P., ... & Fan, Z. (2021). Recent progresses in electrochemical carbon dioxide reduction on copper-based catalysts toward multicarbon products. *Advanced Functional Materials*, *31*(37),   2102151.

(102)   Strmcnik, D., Lopes, P. P., Genorio, B., Stamenkovic, V. R., & Markovic, N. M. (2016). Design principles for hydrogen evolution reaction catalyst materials. *Nano Energy*, *29*, 29-36.

(103)   Lebrun, C., Deniau, G., Tanguy, J., & Lécayon, G. (1996, January). Study of the ability of 4-vinylpyridine to form electropolymerized coatings on nickel cathodes. In *AIP Conference Proceedings* (Vol. 354, No. 1, pp. 67-74). American Institute of Physics.

(104)   Saito, T., Ikeda, H., Matsuda, Y., & Tamura, H. (1973). Cathodic polarization characteristics of poly (4-vinylpyridine) bromine complex. *Journal of Applied Electrochemistry*, *3*(2), 99-102.

(105)   Osaimany, P., Samuel, A. S., Johnbosco, Y., Kharwar, Y. P., & Chakravarthy, V. (2019). A study of synergistic effect on oxygen reduction activity and capacitive performance of NiCo2O4/rGO hybrid catalyst for rechargeable metal-air batteries and supercapacitor applications. *Composites Part B: Engineering*, *176*, 107327.

Poly(1,5-diaminonaphthalene) grafted monolithic 3D hierarchical carbon as highly capacitive and stable supercapacitor electrodes
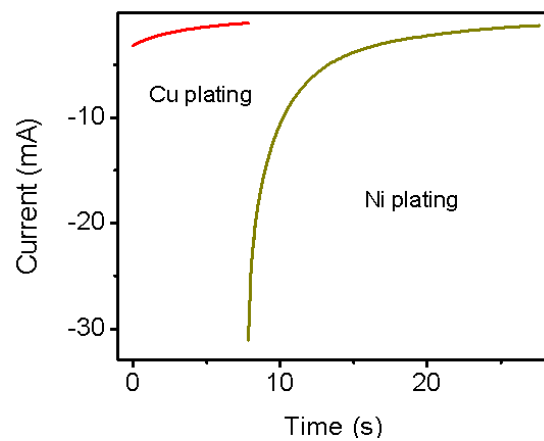
Figure S1. Cu and Ni catalyst deposition at constant potentials of 0,04 V and -0,56 V vs SCE respectively.
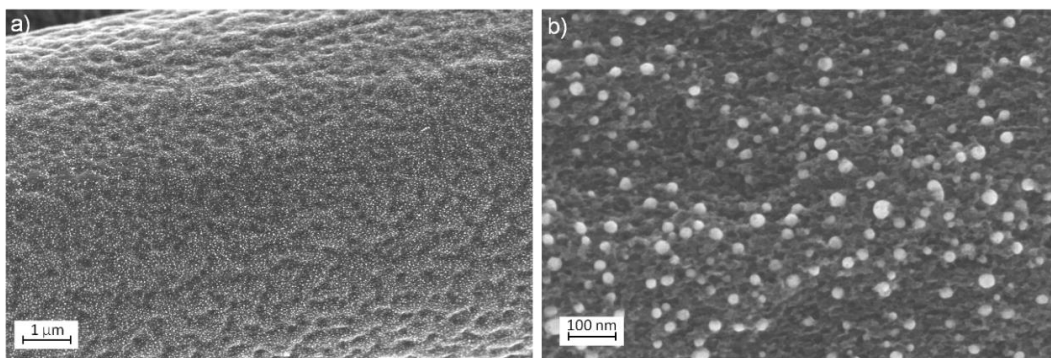
Figure S2 (a-b). SEM images of Ni-Cu catalysts on a-CC surface. Spherical catalysts were obtained with electroplating and annealing in Ar/H_2 atmosphere at 650°C.
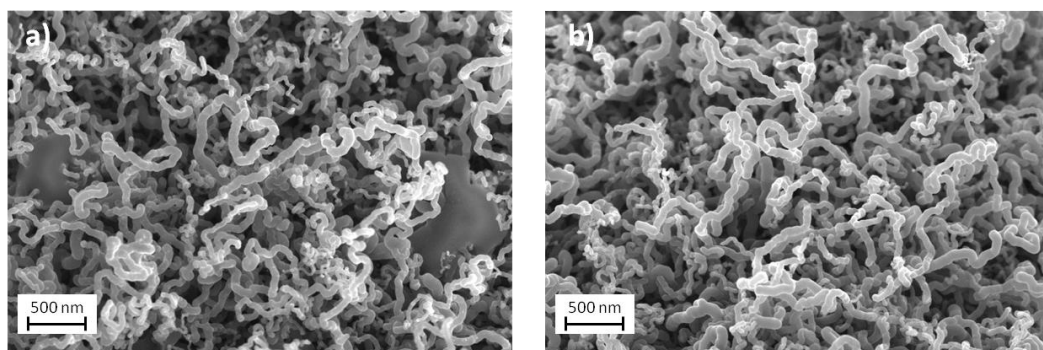
Figure S3. Amorphous carbon removal. SEM images **(a)** before and **(b)** after HNO_3 treatment.

53
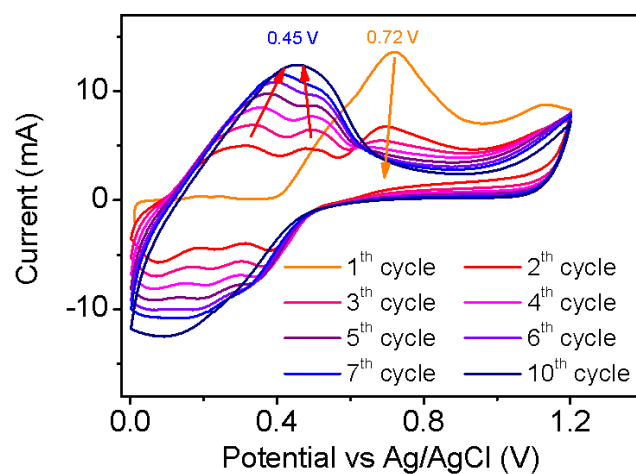
Figure S4. Electro-oxidative polymerization via cyclic voltammetry in acidic medium.
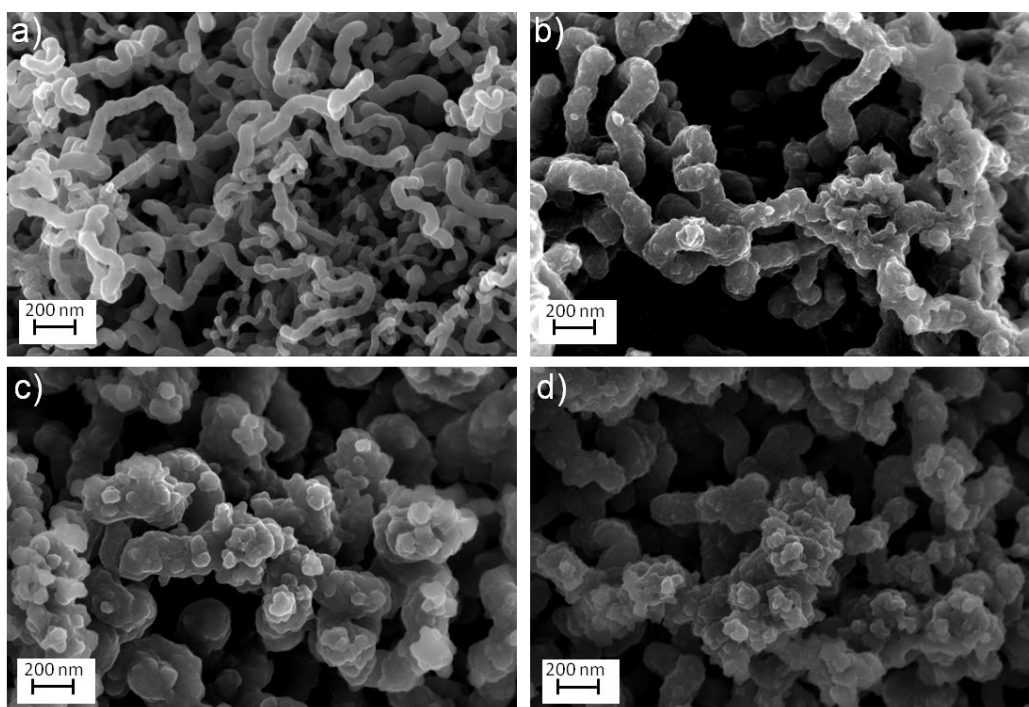
Figure S5. SEM image comparison with different polymerization cycles in acid. **(a)** SEM images with 50kX magnification of CC-a-CC and 1,5 PDAN on CNT-a-CC with **(b)** 5 cycles **(c)** 20 cycles **(d)** 80 cycles.
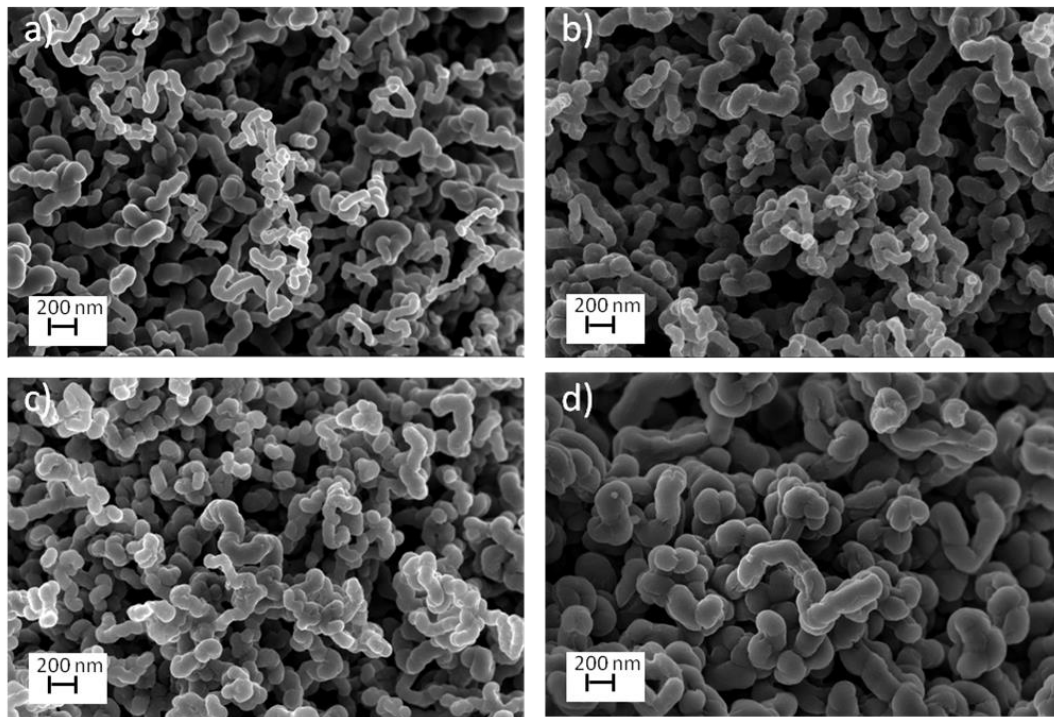
Figure S6. SEM image comparison with different polymerization cycles in acetonitrile **(a)** with 25kX magnification of CC-a-CC and 1,5 PDAN on CNT-a-CC with **(b)** 5 cycles **(c)** 20 cycles **(d)** 40 cycles.
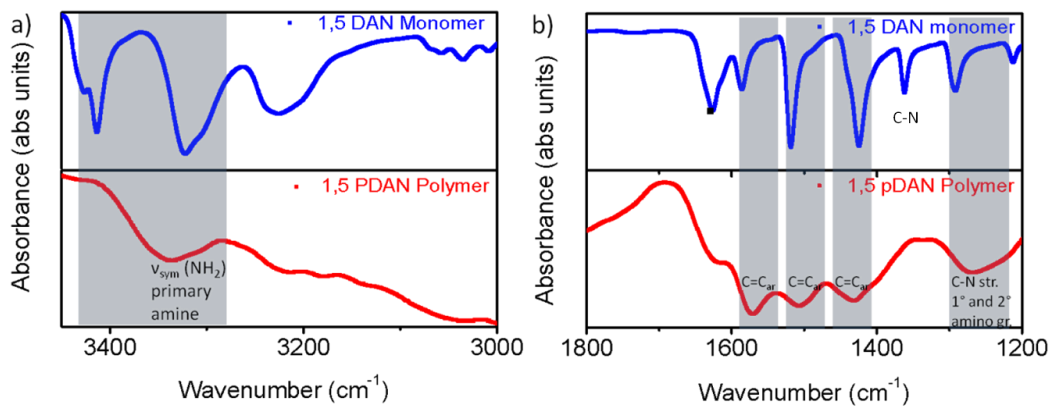
Figure S7 (a-b). FTIR analysis of 1,5 PDAN and distinctive peaks with their possible assignments.
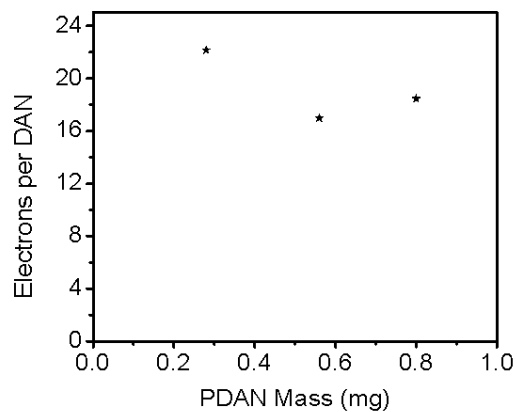
Figure S8. Electrons consumed during polymerization in MeCN for each 1,5 DAN monomers.
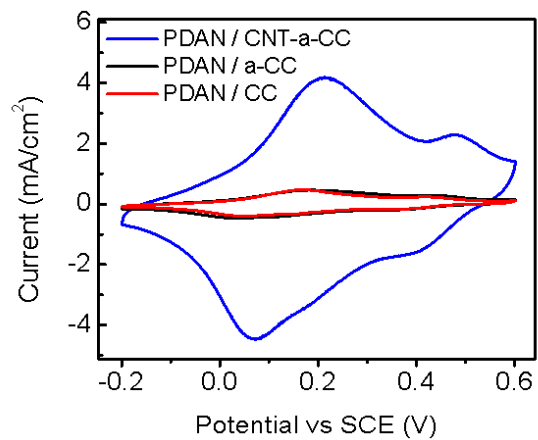
Figure S9. CV analysis of 1,5 PDAN (20 pulses) on various substrates, CC, a-CC and CNT-a-CC at 2 mV/s.
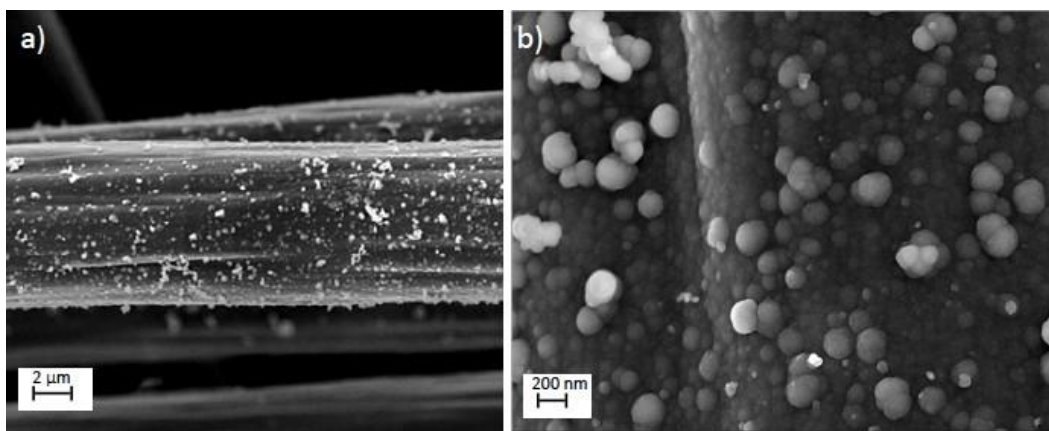
Figure S10 (a-b). SEM images of 0.48 mg/cm²1,5 PDAN on a-CC
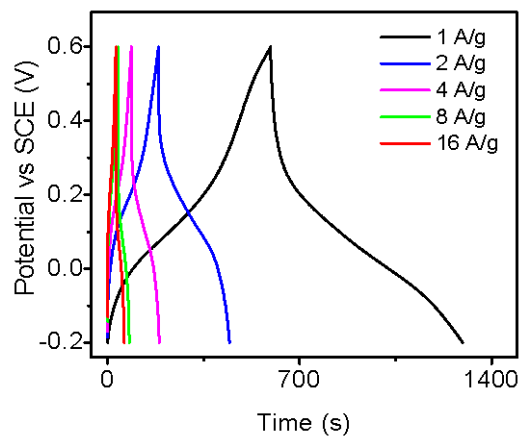
Figure S11. Galvanostatic charge/discharge analysis at different current rates.
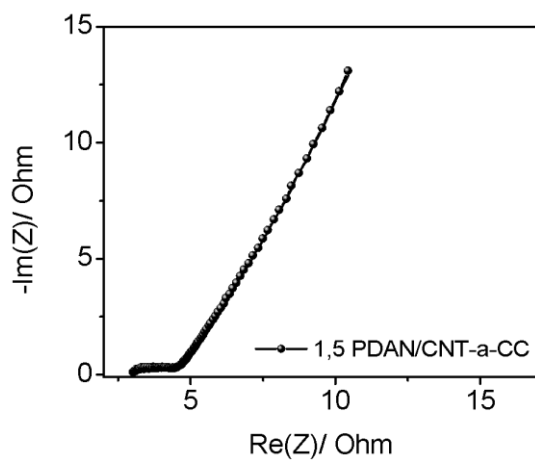
Figure S12. Nyquist plot for 2.5 mg/cm² 1,5 PDAN grafted CNT-a-CC.
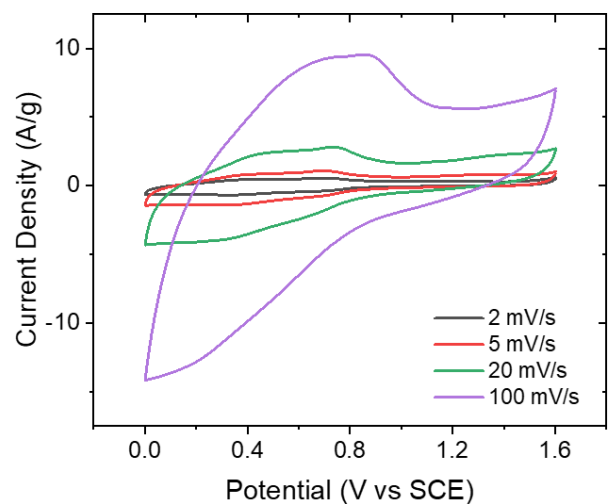
Figure S13. CV profiles of 2-electrode asymmetric cell with 1,5 PDAN grafted on CNT-a-CC as positive electrode and porous carbon as negative electrode in 0.5 M H2SO4.
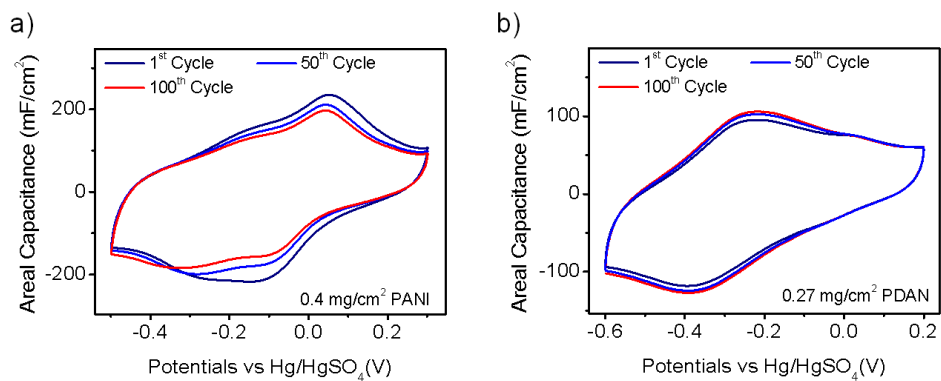
Figure S14. Stability test for **(a)** PANI and **(b)** 1,5 PDAN with subsequent CV scans at 20 mV/s for 100 cycles on a-CC.
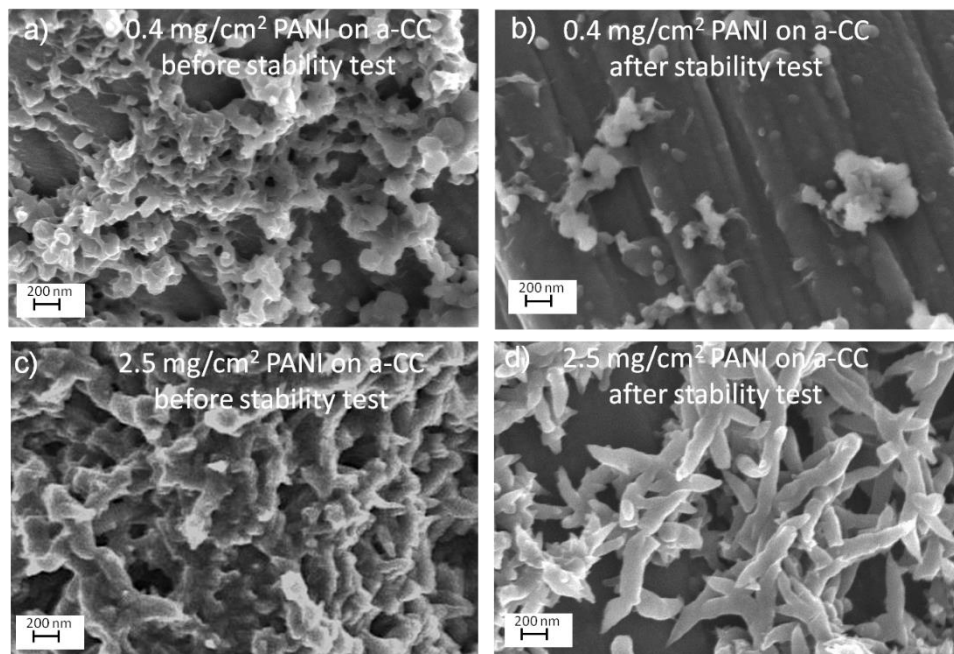
Figure S15. SEM images of PANI on a-CC before (**a-c**) and after stability test (**b-d**).
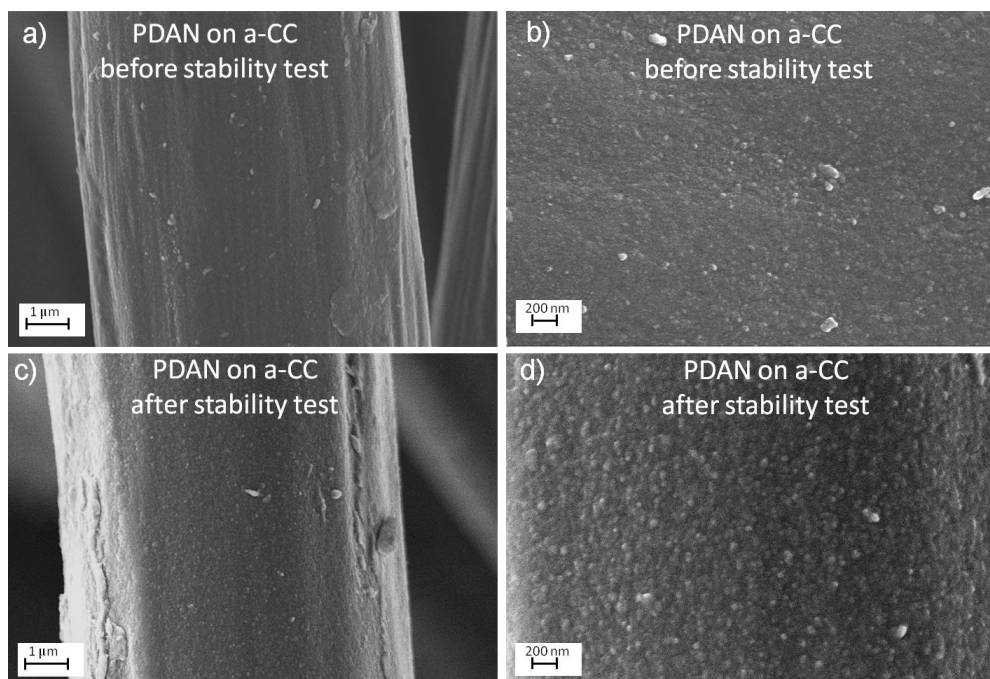
Figure S16. SEM images of 0.27 mg/cm^2 PDAN on a-CC before (**a-b**) and after stability test (**c-d**).